RESEARCH ARTICLE

Rapid Transcription Dynamics Confers Cytarabine Resistance in Acute Myeloid Leukemia

Goichi Tatsumi[1], Rajni Kumari[1], Yutaro Suzuki[1], Shuting Li[1], Russell Scharf[1], Samuel J. Taylor[1], Sriram Sundaravel[1], Amit Verma[2,3,4,5,6,7], Justin C. Wheat[1], and Ulrich Steidl[1,3,4,5,6,7,8]

ABSTRACT Chemotherapy resistance remains a critical challenge in the treatment of patients with cancer, including acute myeloid leukemia (AML). Although genetic alterations can contribute to resistance, the role of rapid-adaptive nongenetic mechanisms, particularly transcription dynamics, remains poorly understood. In this article, we demonstrate that short-term treatment of AML cells with the widely used chemotherapeutic cytarabine (AraC) leads to the rapid emergence of a cell population with significant RNA induction and increased AraC resistance in cell lines and primary patient samples. Mechanistically, transcriptomic and targeted high-resolution analysis of transcription dynamics using single-molecule RNA FISH revealed rapid induction of transcriptional dynamics and upregulation of key transcription factors (TF)—which we term "AraC rapid response TFs." Functionally, short-term pre- and cotreatment with RNA transcription inhibitors suppressed chemotherapy-induced RNA induction and prevented resistance acquisition *in vitro* and *in vivo*. Furthermore, CRISPR-mediated suppression of TFs PU.1 and GATA1 significantly attenuated AraC resistance. Our findings reveal a role of rapid-adaptive transcriptional dynamics in AML chemotherapy resistance.

SIGNIFICANCE: This study reveals a role of rapid-adaptive transcriptional dynamics in AML chemotherapy resistance, highlighting master TFs as key regulators. These insights offer a pharmacologically accessible approach to potentially alleviate the major clinical problem of chemotherapy resistance.

INTRODUCTION

Acute myeloid leukemia (AML) remains a hematologic malignancy with a dismal prognosis, particularly due to its high relapse rate. Despite recent advances in chemotherapy, the 5-year overall survival rate for elderly patients—many of whom are ineligible for intensive bone marrow transplantation—remains below 20% (1, 2). Relapsed and refractory AMLs continue to represent the leading causes of mortality in these patients (3, 4), underscoring the urgent need for novel therapeutic strategies to overcome chemotherapy resistance.

The genetic mechanisms underlying chemotherapy resistance in AML have been extensively investigated, leading to the development of targeted therapies directed at resistance-associated genetic alterations. For example, gilteritinib and ponatinib have shown efficacy against specific mutations induced by chemotherapy, such as FLT3-D835 and BCR::ABL-T315I in BCR::ABL1 AML, respectively (5–7). However, these targeted therapies alone are insufficient to fully eliminate chemotherapy resistance, as highlighted by a meta-analysis indicating that approximately 40% of the relapsed AML cases lack identifiable genetic alterations at the time of relapse (8). This observation suggests that nongenetic mechanisms also play a pivotal role in the acquisition of chemotherapy resistance.

Given the increasing recognition of nongenetic factors in chemotherapy resistance, we sought to investigate the contribution of transcription dynamics to the development of cytarabine (AraC) resistance in AML. Previous studies, including our own, have revealed that rapid transcriptional dynamics and variability play a crucial role in cell fate decisions during development, differentiation, and disease progression using human cancer cell lines and primary stem cells from mouse models (9–14), raising the possibility that transcriptional plasticity may also contribute to the acquisition of chemotherapy resistance. Although reports have linked transcriptional variability to drug resistance in solid tumors, such as melanoma, breast cancer, and prostate cancer (15–17), such mechanisms have not yet been systematically explored in the context of leukemia treatment.

AraC remains a cornerstone of AML chemotherapy, with well-characterized mechanisms of action and metabolism (18, 19). However, the precise molecular mechanisms by which AML cells acquire resistance to AraC and how these processes can be therapeutically reversed remain incompletely understood. To address this gap, we investigated the role of transcription dynamics following AraC treatment, aiming to uncover novel strategies to mitigate AraC resistance.

[1]Department of Cell Biology, Albert Einstein College of Medicine, Bronx, New York. [2]Department of Developmental and Molecular Biology, Albert Einstein College of Medicine, Bronx, New York. [3]Montefiore Einstein Comprehensive Cancer Center, Albert Einstein College of Medicine, Montefiore Einstein, Bronx, New York. [4]Blood Cancer Institute, Montefiore Einstein Comprehensive Cancer Center, Albert Einstein College of Medicine, Bronx, New York. [5]Cancer Dormancy Institute, Montefiore Einstein Comprehensive Cancer Center, Albert Einstein College of Medicine, Bronx, New York. [6]Department of Oncology, Albert Einstein College of Medicine, Montefiore Einstein, Bronx, New York. [7]Ruth L. and David S. Gottesman Institute for Stem Cell Research and Regenerative Medicine, Albert Einstein College of Medicine, Bronx, New York. [8]Department of Medicine, Albert Einstein College of Medicine, Montefiore Einstein, Bronx, New York.

G. Tatsumi and R. Kumari contributed equally to this article.

Corresponding Author: Ulrich Steidl, Albert Einstein College of Medicine, 1300 Morris Park Avenue, Bronx 10461, NY. E-mail: ulrich.steidl@einsteinmed.edu

Blood Cancer Discov 2026;XX:1–18

doi: 10.1158/2643-3230.BCD-25-0317

We discovered that exposure to AraC triggers a rapid RNA induction response in AML cells, which plays a key role in the transcription dynamics-mediated resistance acquisition. Importantly, pharmacologic inhibition of transcription, administered both before and during AraC treatment, effectively suppressed this RNA induction, thereby restoring AraC sensitivity to baseline levels. Through high-resolution transcriptional analysis, including at a single-molecule level, we identified master transcription factors (TF), including PU.1 and GATA1, that were rapidly activated within 1 day of AraC treatment. The suppression of these "AraC rapid response master TFs" (ARR-TF) significantly attenuated the acquisition of resistance, providing evidence that the rapid transcription dynamics of master TFs contribute directly to early-stage chemotherapy resistance. Combining AraC with RNA transcription inhibitors significantly prolonged tumor suppression in AML xenograft models *in vivo*, highlighting the therapeutic potential of this combination therapy. Overall, our study identifies rapid transcription dynamics as an essential driver of early AraC resistance and provides a rationale for transcription-targeted combination therapies to mitigate chemotherapy resistance in AML.

RESULTS

Short-term RNA Induction Is Responsible for the Early Acquisition of Adaptive AraC Resistance

To identify and study nongenetic mechanisms of chemotherapy resistance, we initially tested the effect of short-term AraC treatment on multiple human AML cell lines (HL60, NB4, and MOLM14). Cells treated once with an ~IC_{95} dose of AraC (250 nmol/L for HL60 and 500 nmol/L for NB4 and MOLM14, respectively) for 3 days (days 0–3) acquired moderate but significant AraC resistance in all cell types, measured at a time point when cell growth was recovered (on day 14), and remained stable even at day 28 (Fig. 1A; Supplementary Fig. S1A). Interestingly, even a very short 1-day treatment of cells with the same dose of AraC led to significant resistance on day 28 (Supplementary Fig. S1B).

To test whether AraC-treated cells acquired major genetic alterations after short-term AraC treatment, we treated HL60 cells once with 250 nmol/L of AraC for 3 days and performed whole-exome sequencing (WES) on day 14. We did not observe selection or emergence of any dominant genetic clones. The variant allele frequencies of both control and treated cells were highly correlated (Pearson R = 0.961; Supplementary Fig. S2A). We observed relatively few genetic alterations [three insertions/deletions (InDel) and 30 single-nucleotide variants (SNV)] after AraC treatment (Supplementary Table S1). All variants were at low frequencies and in genes not previously reported to be associated with AraC resistance, to the best of our knowledge, indicating that no major clones with resistance-related gene alterations were acquired and selected under the short-term treatment conditions.

As these results indicated that very short-term exposure to AraC is sufficient to generate resistance driven by adaptive nongenetic mechanisms, we next investigated RNA transcription dynamics after AraC treatment. We first assessed the changes in RNA synthesis activity using nascent RNA labeling with ethynyl uridine (EU), a uridine analog that incorporates only into newly transcribed RNA. Strikingly, a sizable majority of cells showed more active nascent RNA transcription 1 day after AraC treatment compared with the untreated control in all three cell lines HL60, NB4, and MOLM14 (Fig. 1B). Next, we combined RNA and cell-cycle analyses to monitor the changes in RNA expression levels. As cells undergoing mitosis are effectively targeted by AraC treatment (20, 21), we restricted this analysis to cells in the G_0–G_1 cell-cycle phase. The RNA expression levels of cells in the G_0–G_1-phase increased significantly and rapidly after 3 days of AraC treatment and returned to steady state soon after treatment withdrawal, even though AraC-treated cells continued to display resistance to AraC (Fig. 1C; Supplementary Fig. S1C, S1D, and S1E). An alternative method of RNA staining with SYTO RNASelect dye, instead of pyronin Y, showed an increase in overall RNA levels at day 1 after treatment as well, although the measurements were not quantified (Supplementary Fig. S1F). These data indicate that RNA induction is a consistent phenomenon following short-term AraC treatment.

To evaluate the functional role of the RNA-induced cell population emerging after AraC treatment, we flow-sorted pyronin Y high (PY^{High}) and low (PY^{Low}) cells 1 day after AraC treatment and examined AraC sensitivity after cell growth recovery (Fig. 1D). Strikingly, PY^{High} cells were significantly more resistant to AraC than PY^{Low} cells (Fig. 1E; Supplementary Fig. S1G), suggesting that RNA induction after AraC treatment is functionally relevant for the acquisition of rapid resistance to AraC.

To evaluate whether specific genetically defined clones expand within this RNA-high subpopulation, we performed whole-exome analysis of flow-sorted PY^{High} and PY^{Low} cells. Consistent with the analysis of unfractionated cells, we did not observe the emergence or selection of any genetic mutations in either PY^{High} or PY^{Low} cells (Pearson R = 0.958; Supplementary Fig. S2B).

Suppression of mRNA Induction Prevents the Early Acquisition of Resistance to AraC

To further understand the role of RNA induction after AraC treatment in association with resistance, we tested the impact of preventing RNA induction with four different RNA transcription inhibitors: actinomycin D (ActD), BET protein degrader (dBET6), CX5461, and ellipticine. ActD disrupts all types of RNA synthesis (22), whereas dBET6 selectively inhibits the activation of mRNA transcription by blocking the assembly of the RNA polymerase II (Pol II) elongation complex (23, 24). In contrast, CX5461 and ellipticine are both RNA polymerase I (Pol I) inhibitors, which interrupt ribosomal RNA (rRNA) synthesis (25, 26).

To investigate the impact of these RNA transcription inhibitors on AraC-induced RNA induction, we pretreated HL60 cells with 500 pmol/L of ActD, 5 nmol/L of dBET6, 10 nmol/L of CX5461, or 10 nmol/L of ellipticine, respectively, to exert functional effects with a minimal impact on cell growth (~20% growth inhibition). After pretreatment with RNA transcription inhibitors for 3 days, combination treatment with AraC and RNA transcription inhibitors was

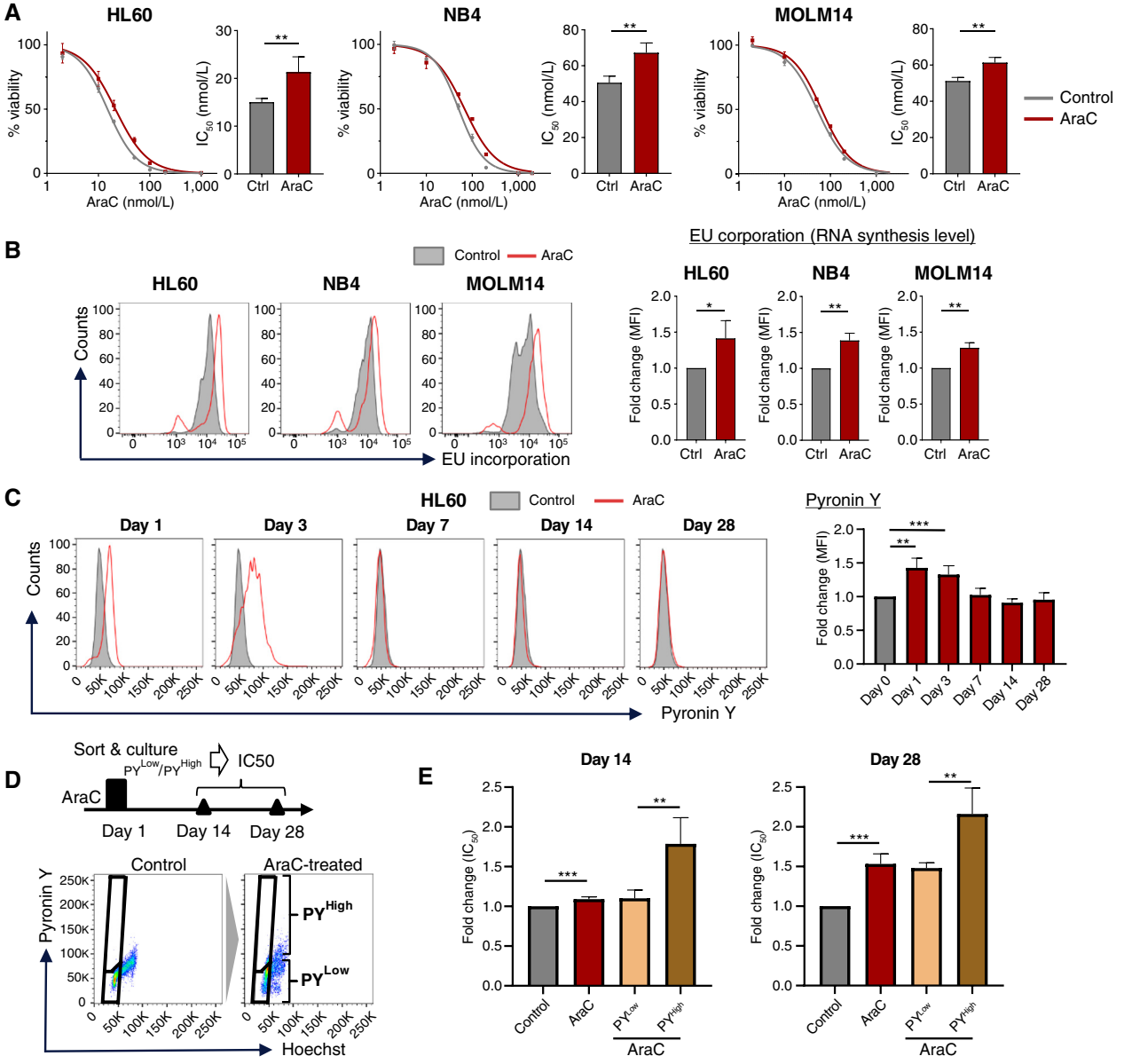

Figure 1. RNA induction after AraC treatment is involved in the acquisition of AraC resistance. **A,** Dose–response curves of HL60, NB4, and MOLM14 proliferation for AraC ($n = 4$; technical replicates) on day 14. The cells were treated with 250 nmol/L of AraC for HL60 and 500 nmol/L of AraC for NB4 and MOLM14 for 3 days. Experimental replicates displayed mean ± SD. The bar charts show IC_{50} (mean ± SD) values for AraC for each cell ($n = 4$; technical replicates). **, $P < 0.01$ via unpaired *t* test. **B,** Representative flow cytometry histogram of RNA synthesis using ethynyl uridine (EU) labeling on HL60, NB4, and MOLM14 cells after a 1-day treatment with the same doses of AraC as above or DMSO. Live cells were selected by DAPI staining for this analysis, and the *x*-axis displays the fluorescence intensity of EU incorporation, indicating RNA synthesis activity levels. The bar charts show the summary fold changes in the EU mean fluorescent intensity (MFI) data following DMSO or AraC treatment for each cell ($n = 3$; technical replicates). *, $P < 0.05$; **, $P < 0.01$ via unpaired *t* test. **C,** Representative flow cytometry histogram of RNA expression using pyronin Y on HL60 on days 1, 3, 7, 14, and 28, after a 3-day treatment with 250 nmol/L of AraC. Live cells in the G_0–G_1 cell-cycle phase were selected by Hoechst 33342 staining, and the *x*-axis displays the fluorescence intensity of pyronin Y, indicating RNA content levels. The bar chart shows summary fold changes of MFI data following DMSO or AraC at each time point ($n = 3$–4; technical replicates). **, $P < 0.01$; ***, $P < 0.001$ via unpaired *t* test. **D,** Experimental schematic for assessing the differences in AraC sensitivity of pyronin Y–sorted cells. Representative flow cytometry data of control and AraC-treated cells are shown at the bottom, and the PY^{High} gate is defined as the area in which the number of cells is <1% in the control within the G_0–G_1 cell-cycle phase. **E,** Changes in AraC sensitivity in HL60 on days 14 and 28 following a 1-day treatment with 250 nmol/L of AraC, among untreated control and AraC-treated cells, and PY^{Low}- and PY^{High}-sorted populations within AraC-treated cells. The fold changes in IC_{50} values were calculated at each time point by dividing the IC_{50} of AraC-treated cells, PY^{Low}-, and PY^{High}-sorted cells by that of the control ($n = 4$; technical replicates). **, $P < 0.01$; ***, $P < 0.001$ via unpaired *t* test. Ctrl, control.

performed for 1 day (Supplementary Fig. S3A). RNA synthesis, as measured by EU incorporation, significantly decreased in HL60 cells following combination treatment with AraC and ActD or dBET6 (to 21% and 27% of the AraC-treated cells, respectively; Fig. 2A). Surprisingly, there were only minimal changes in RNA synthesis when treated with AraC and RNA

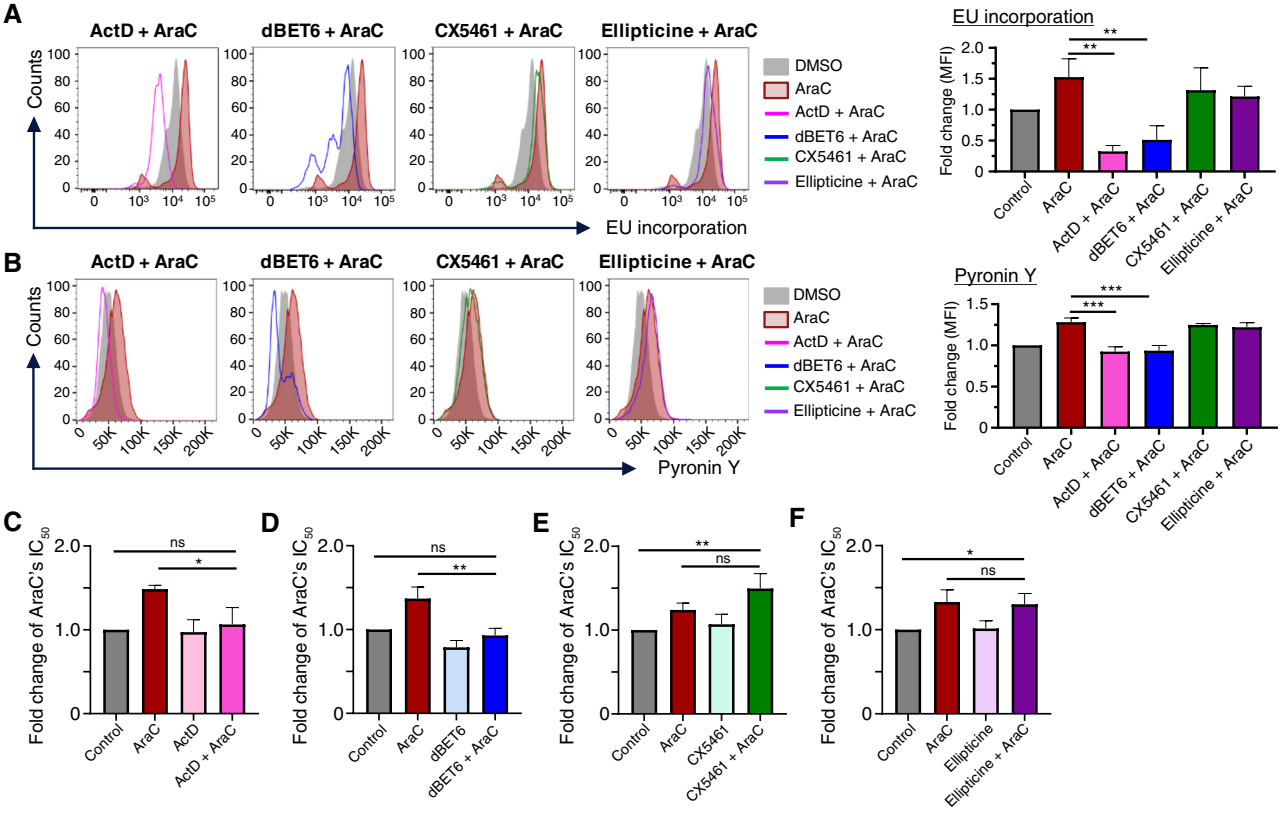

Figure 2. Suppression of RNA induction triggered by AraC can prevent the acquisition of AraC resistance. **A** and **B,** Representative flow cytometry histograms of RNA synthesis using ethynyl uridine (EU) labeling (**A**) and RNA amount using pyronin Y (**B**) in HL60 cells after a 3-day pretreatment with 500 pmol/L of ActD, 5 nmol/L of dBET6, 10 nmol/L of CX-5461, or 10 nmol/L of ellipticine and an additional 1-day cotreatment with 250 nmol/L of AraC and each drug at the same dose. All data were overlaid with data from DMSO control and AraC-treated cells (1 day). Dead cells were excluded by selecting live cells using DAPI (**A**) or Hoechst 33342 (**B**). The bar charts summarize the fold changes in mean fluorescent intensity (MFI) values following each drug treatment. For (**A** and **B**), the fold changes were calculated by dividing the MFI of treated cells by that of DMSO control cells ($n = 3$; technical replicates). **, $P < 0.01$; ***, $P < 0.001$ via unpaired t test. **C–F,** Changes in AraC sensitivity on day 28, after a 3-day pretreatment with 500 pmol/L of ActD (**C**), 5 nmol/L of dBET6 (**D**), 10 nmol/L of CX-5461 (**E**), and 10 nmol/L of ellipticine (**F**), and an additional 3-day cotreatment with 250 nmol/L of AraC and each drug at the same dose. The fold changes in the IC_{50} values were calculated by dividing the IC_{50} of each treated cell group by that of the control ($n = 3$–4; technical replicates). *, $P < 0.05$; **, $P < 0.01$ via unpaired t test. ns, not significant.

Pol I inhibitors (86% and 80% of the AraC-treated cells with CX5461 or ellipticine, respectively), even though pre-rRNA levels were significantly suppressed after 3 days of treatment with only the RNA Pol I inhibitors (Fig. 2A and B; Supplementary Fig. S3B). Similarly, overall RNA expression levels, as measured by pyronin Y, decreased and returned to the control-treated [dimethyl sulfoxide (DMSO)] HL60 cells' level after combination treatment with AraC and ActD or dBET6 (72% and 73% of AraC-treated cells, respectively), whereas there were no significant changes when AraC was combined with RNA Pol I inhibitors (98% and 93% of AraC-treated cells in CX5461 and ellipticine, respectively; Fig. 2B). These results were consistent across two other AML cell lines (Supplementary Fig. S3C and S3D), indicating that the induced RNA was transcribed by RNA Pol II and could therefore be blocked by pre- and cotreatment with ActD and dBET6, but not with RNA Pol I inhibitors.

Subsequently, to test whether the inhibition of RNA induction can mitigate the development of AraC resistance, we assessed AraC sensitivity after a 3-day pretreatment with RNA transcription inhibitors and a 3-day cotreatment with AraC and RNA transcription inhibitors (Supplementary Fig. S3A). Strikingly, combination treatment with AraC and ActD or dBET6 improved AraC sensitivity to the level of untreated controls 28 days after treatment, whereas RNA Pol I inhibitors had no significant effect on AraC resistance (Fig. 2C–F; Supplementary Fig. S3E–S3H). These data highlight that enhanced mRNA transcription by RNA Pol II is causative for the development of rapid and early resistance to AraC and that suppression of mRNA elevation can prevent the early acquisition of AraC resistance in AML cells.

Preemptive Inhibition of mRNA Transcription Enhances the Antileukemic Efficacy of AraC *In Vivo*

To test the effect of mRNA transcription inhibition on AraC treatment *in vivo*, we subcutaneously transplanted HL60 or NB4 cells into NOD.Cg-*Prkdc*^{scid} *Il2rg*^{tm1Wjl}/SzJ (NSG) mice and monitored the changes in leukemia cell growth upon treatment with AraC alone or pre- and cotreatment with the RNA Pol II transcription inhibitor dBET6 (see the "Methods" section for details). Leukemia cell growth was not significantly different in control mice or mice treated with dBET6

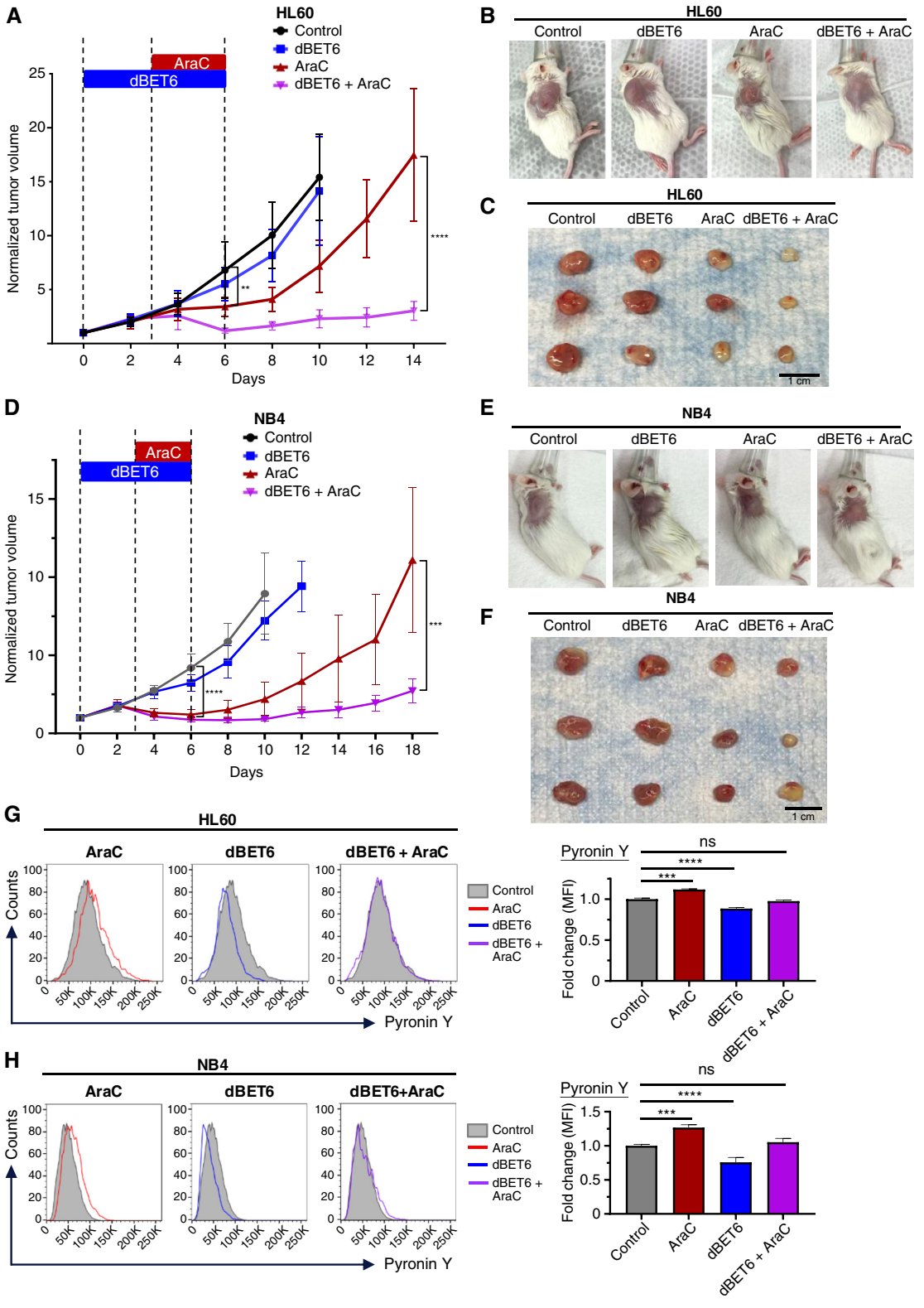

Figure 3. Suppression of AraC-induced RNA induction by dBET6 provides longer tumor growth prevention in an *in vivo* tumor model. **A,** Tumor growth curve in subcutaneously HL60-transplanted NSG mice treated at the site of the tumor with dBET6 (150 μg/tumor/day, days 1–6), AraC (2 mg/tumor/day, days 4–6), or both ($n = 7$–8 for each condition; biological replicates). Normalized tumor volume indicates the relative volume when the tumor volume at day 0 (at the start of dBET6) is set to 1. **, $P < 0.01$; ****, $P < 0.0001$ via unpaired *t* test. **B** and **C,** Representative photographs of subcutaneous tumors in NSG mice (**B**) and excised HL60 cell tumors (**C**) on day 6 (immediately after all treatments were completed) from the experiment in (**A**). (*continued on following page*)

alone, whereas leukemia cell growth was modestly but significantly inhibited in AraC-treated mice at the end of AraC treatment (day 6). Mice treated with dBET6 + AraC showed even greater inhibition of leukemia cell growth at that time point [P <0.01 (HL60) and P <0.0001 (NB4); Fig. 3A–F]. Strikingly, after AraC withdrawal, the leukemia-inhibitory effect of AraC did not persist, and growth accelerated immediately in mice treated with AraC only. In contrast, mice treated with dBET6 + AraC showed sustained inhibition of leukemia cell growth for about 14 days (HL60) and 16 to 18 days (NB4), respectively (Fig. 3A and E). At that time point, leukemia cell growth in dBET6 + AraC–treated mice was only 17% (HL60) or 36% (NB4) of that in AraC-treated mice, and this difference was highly statistically significant [P <0.0001 (HL60) and P = 0.0004 (NB4); Fig. 3A and D].

The analysis of RNA expression levels in leukemia cells at the end of AraC treatment (day 6) showed that global RNA was upregulated in AraC-treated tumor cells *in vivo* [112% (HL60, P <0.0001) and 127% (NB4, P <0.0001) of the untreated control; Fig. 3G and H], similar to our findings in *ex vivo* models (Fig. 2). In contrast, leukemia cells in AraC + dBET6–treated mice showed restored RNA levels back to the same levels as in untreated mice [98% (HL60, P >0.05) and 105% (NB4, P >0.05) of the untreated control; Fig. 3G and H]. Taken together, these data show that preemptive suppression of mRNA induction prior to and concurrent with AraC treatment led to significantly enhanced AraC sensitivity and a longer-lasting antileukemic effect *in vivo*.

ARR-TF Signatures are Activated after AraC Treatment

To explore the global mRNA transcriptomic changes associated with the acquisition of AraC resistance, we performed RNA sequencing (RNA-seq) on control untreated cells and 1-day 250 nmol/L AraC-treated HL60 cells in the G_0–G_1 cell-cycle phase (Fig. 4A and B). We detected significant differences in the expression of a subset of genes between the control and AraC-treated cells (Fig. 4B). Gene set enrichment analysis (GSEA) revealed signatures associated with TF DNA-binding activities that were enriched in AraC-treated cells, indicating that TF activities seemed to be increased following AraC treatment (Supplementary Fig. S4A). Dynamic changes in TF expression and regulation networks have been shown to be key to switching fates, such as differentiation block and cell death inhibition, in drug resistance (27). Therefore, we next investigated the changes in the gene regulatory network of key hematopoiesis-related TFs following AraC treatment. Interestingly, GSEA showed that the target signatures of several master TFs for hematopoiesis, such as PU.1, GATA1, RUNX1, and CEBPA, were enriched in AraC-treated cells compared with untreated control cells (Fig. 4C), whereas the signatures of some other TFs, such as FOXO4 and MYC, were attenuated in AraC-treated cells (Supplementary Fig. S4B). This suggested the possibility that some TFs, which we will refer to as ARR-TFs, are specifically involved in the rapid acquisition of nongenetic AraC resistance. Of note, bulk RNA-seq failed to detect changes in the expression of these TFs, and some TFs like GATA1 were below the detection limit (Supplementary Fig. S4C). Next, we performed single-cell RNA-seq (scRNA-seq) on PY^{High} and PY^{Low} HL60 cells and did not observe transcriptionally distinct populations between these two fractions in Uniform Manifold Approximation and Projection (UMAP) analysis (Supplementary Fig. S4D). This suggested that the global transcriptomic differences between these states are subtle and may be masked by the high noise-to-signal ratio inherent to droplet-based single-cell platforms. Notably, many ARR-TFs were only borderline or not at all detectable because of their low expression levels (Supplementary Fig. S4E). Specifically, GATA1, FOXO4, and HOXA11 were not detectable in the scRNA-seq dataset. Despite these sensitivity issues at the level of individual TFs, we observed a significant increase in PU.1 and GATA1 target gene scores in the PY^{High} fraction, accompanied by significantly upregulated expression of individual target genes (Supplementary Fig. S4F and S4G). We also observed subtle yet significant increases in RUNX1 and CEBPA target gene scores, with several of their downstream targets showing significantly higher expression in the PY^{High} fraction (Supplementary Fig. S4H and S4I).

Transcription Burst Frequency of ARR-TFs is Increased after AraC Treatment

To examine TF dynamics following AraC treatment at the highest possible resolution, we performed single-molecule RNA fluorescence *in situ* hybridization (smFISH) for ARR-TFs and other TFs as controls. The smFISH is the gold standard technique for examining transcriptional bursting at the highest resolution. We first assessed the transcription dynamics of ARR-TFs, PU.1, GATA1, RUNX1, and CEBPA in HL60 cells, 1 day after 250 nmol/L AraC treatment, and found that mature mRNA levels of each of these TFs were significantly elevated (Fig. 4D and E). We also observed a significant increase in transcription site (TS) burst frequency (27%, 1.0%, 6.4%, and 17% of cells with active TS bursting sites increased to 62%, 3.4%, 69%, and 39%, respectively; Fig. 4F) and total nascent

Figure 3. ***(Continued)*** Scale bars, 1 cm. **D,** Tumor growth curve in subcutaneously NB4-transplanted NSG mice treated with dBET6 (50 μg/tumor/day, days 1–6), AraC (3 mg/tumor/day, days 4–6), or both at the site of the tumor (n = 7–8 for each condition; biological replicates). Normalized tumor volume indicates the relative volume when the tumor volume at day 0 (at the start of dBET6) is set to 1. ***, P <0.001; ****, P <0.0001 via unpaired t test. **E** and **F,** Representative photographs of subcutaneous tumors in NSG mice (**E**) and excised tumors of NB4 cells (**F**) on day 6 (immediately after all treatments are completed), from the experiment in (**D**). Scale bars, 1 cm. **G,** Representative flow cytometry histogram of RNA expression using pyronin Y on tumor cells from xenografts in NSG mice on day 6. Live cells in the G_0–G_1 cell-cycle phase were selected by Hoechst 33342 staining, and the x-axis displays the fluorescence intensity of pyronin Y. The bar chart shows summary fold changes of mean fluorescent intensity (MFI) data following DMSO, AraC, dBET6, or both (n = 3 for each condition; biological replicates), compared with the DMSO control. ***, P <0.001; ****, P <0.0001 via unpaired t test. **H,** Representative flow cytometry histogram of RNA expression using pyronin Y on tumor cells from xenograft in NSG mice on day 6. Live cells in the G_0–G_1 cell-cycle phase were selected by Hoechst 33342 staining, and the x-axis displays the fluorescence intensity of pyronin Y. The bar chart shows summary fold changes of MFI data following DMSO, AraC, dBET6, or both (n = 3 for each condition; biological replicates), compared with the DMSO control. ***, P <0.001; ****, P <0.0001 via unpaired t test.

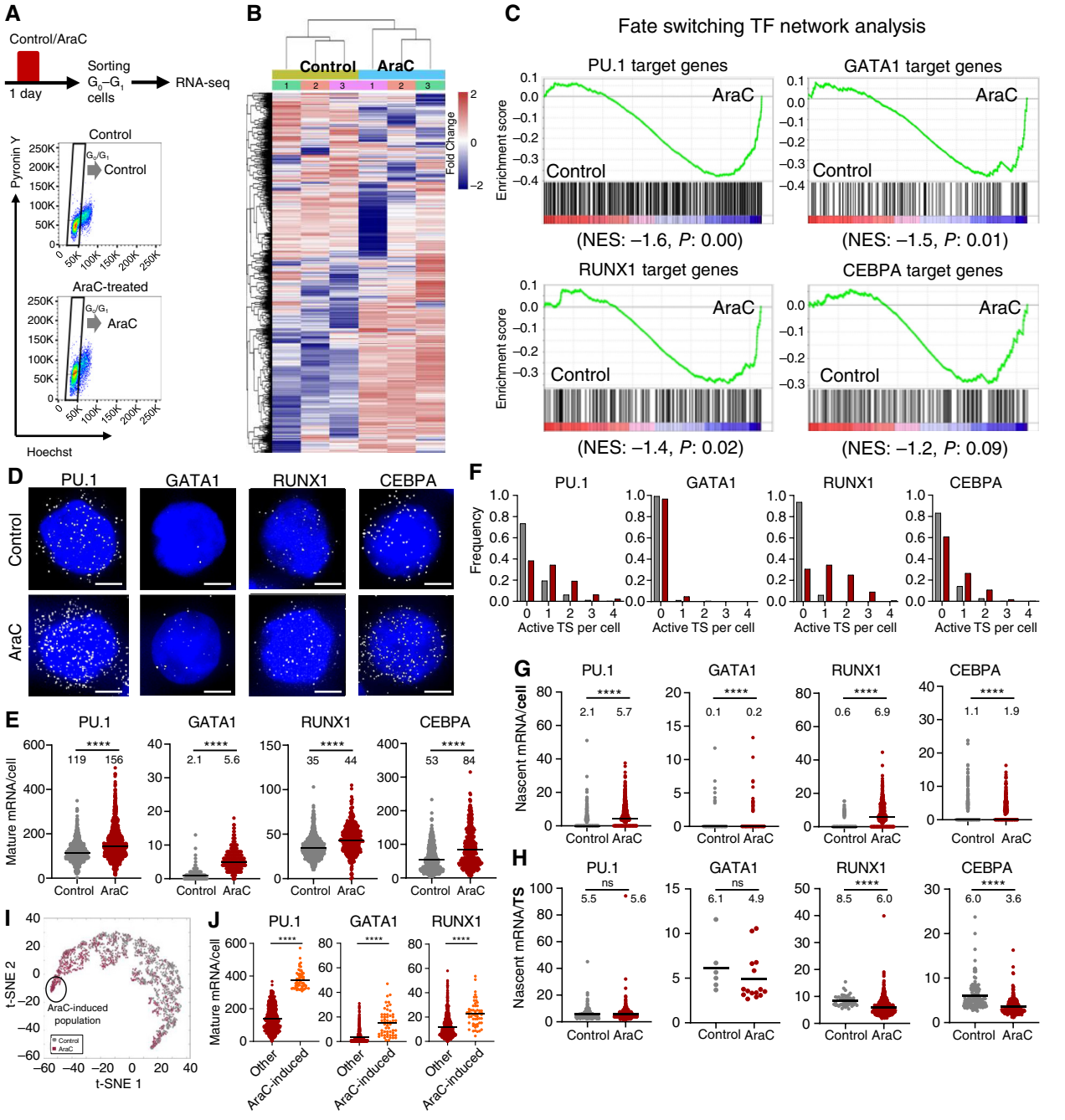

Figure 4. "AraC response" master TFs are rapidly activated after AraC treatment. **A,** Experimental schematic for comprehensively assessing gene profiling differences between control and AraC-treated cells within the G_0–G_1 cell-cycle phase. HL60 cells were treated with AraC for 1 day and subsequently subjected to mRNA-seq. **B,** Heatmap visualization of mRNA-seq data from (**A**) showing global transcriptomic changes in G_0–G_1 cells of HL60 control and cells treated with 250 nmol/L of AraC for 1 day ($n = 3$; technical replicates). **C,** GSEA of PU.1, GATA1, RUNX1, and CEBPA target gene sets in a control vs. AraC-treated experiment (**A**). **D,** Representative smFISH images for PU.1, GATA1, RUNX, and CEBPA in control (top; DMSO) and 250 nmol/L of AraC-treated (bottom) HL60 cells following a 1-day treatment. TF transcripts are in white pseudocolor; DNA is in blue pseudocolor. Scale bars, 5 μm. **E,** Violin plots depicting mature mRNA counts per cell for PU.1, GATA1, RUNX1, and CEBPA in control and AraC-treated HL60 cells. The cells were treated with DMSO or 250 nmol/L of AraC for 1 day. Numbers and horizontal bars indicate mean values. ****, $P < 0.0001$ via nonparametric Mann–Whitney U test. **F,** TS burst frequency per cell for PU.1, GATA1, RUNX, and CEBPA in control (DMSO) and 250 nmol/L of AraC-treated HL60 cells following a 1-day treatment (pooled data of $n = 3$; technical replicates). **G** and **H,** Number of nascent mRNA molecules per cell (**G**) and nascent mRNA molecules per TS (**H**) for PU.1, GATA1, RUNX, and CEBPA in control (DMSO) and 250 nmol/L of AraC-treated HL60 cells following a 1-day treatment. Numbers and horizontal bars indicate mean values. ****, $P < 0.0001$ via nonparametric Mann–Whitney U test. **I,** t-SNE visualization of PU.1, GATA1, and RUNX1 transcript datasets simultaneously acquired in multiplex smFISH experiments. Each dot represents an individual cell colored as follows: control cells in gray and AraC-treated cells in dark red. The population with a unique expression status of PU.1, GATA1, and RUNX1 that emerged only in AraC-treated cells is circled by a black line. **J,** Violin plots depicting mature mRNA counts per cell for PU.1, GATA1, and RUNX1 in the AraC-induced population extracted from t-SNE (**I**) and the other population within AraC-treated HL60 cells. Horizontal bars indicate mean values. ****, $P < 0.0001$ via nonparametric Mann–Whitney U test. NES, normalized enrichment score; ns, not significant.

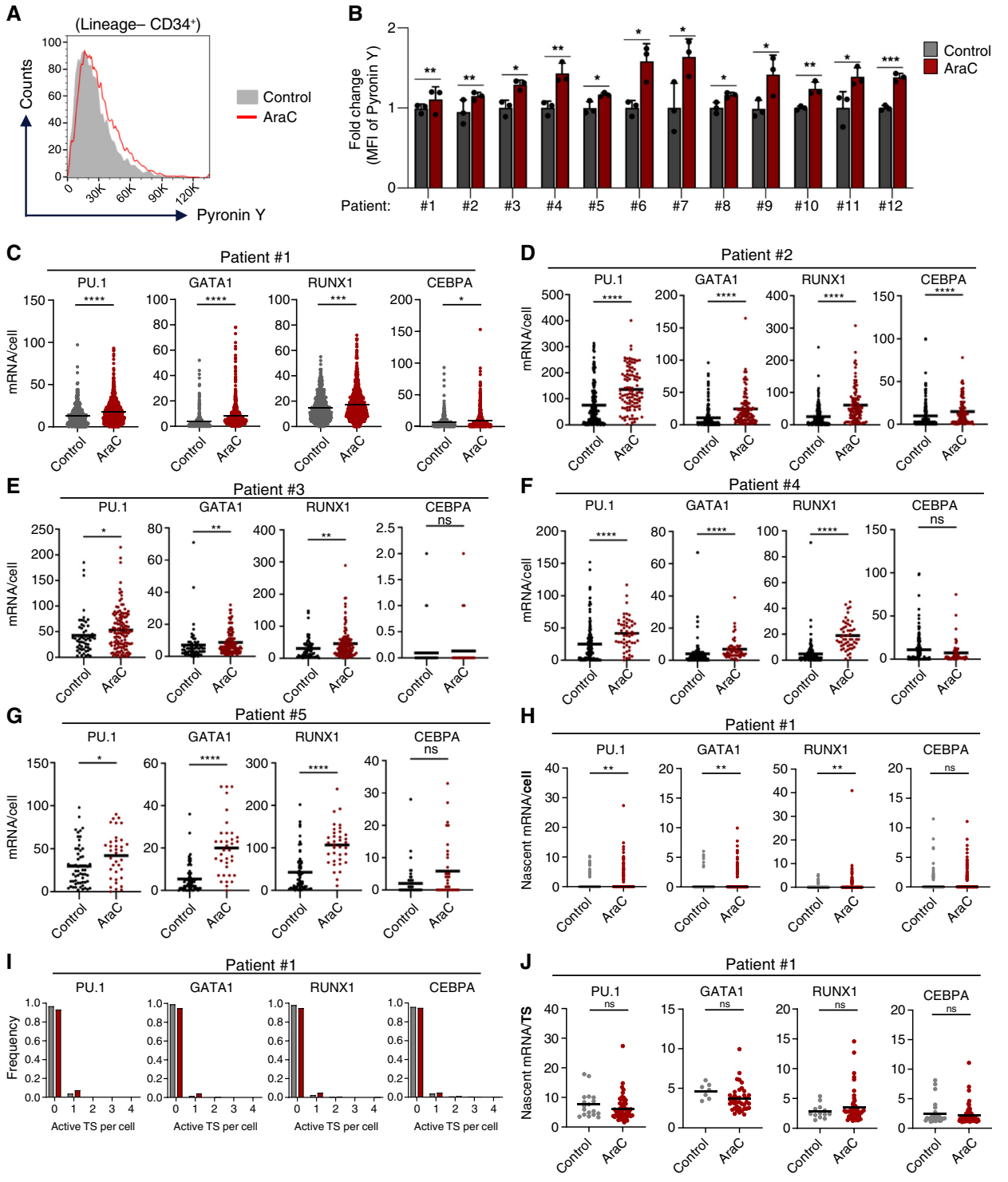

Figure 5. RNA induction and elevated "AraC response" TFs following AraC treatment in cells of patients with primary AML. **A,** Representative flow cytometry histogram of RNA expression using pyronin Y in HSPCs (Lineage—CD34+ fraction) of leukapheresis samples from patients with primary AML after a 1-day treatment with 1 μmol/L of AraC or DMSO *in vitro*. **B,** The bar charts show summary fold changes of mean fluorescent intensity (MFI) of pyronin Y data following DMSO or AraC for each patient ($n = 3$; technical replicates). *, $P < 0.05$; **, $P < 0.01$ via unpaired *t* test. **C–G,** Violin plots depicting mature mRNA counts per cell for PU.1, GATA1, RUNX1, and CEBPA in control (DMSO) and 1 μmol/L of AraC-treated cells from patients 1 to 5 (shown in **B**). Cells were treated with 1 μmol/L of AraC or DMSO for 1 day. Numbers and horizontal bars indicate mean values. *, $P < 0.05$; ***, $P < 0.001$; ****, $P < 0.0001$ via nonparametric Mann–Whitney *U* test. **H,** TS burst frequency per cell for PU.1, GATA1, RUNX, and CEBPA in control (DMSO) and 1 μmol/L of AraC-treated cells following 1 day of treatment, in cells from patient 1. **I** and **J,** Number of nascent mRNA molecules per cell (**E**) and nascent mRNA molecules per TS (**F**) for PU.1, GATA1, RUNX, and CEBPA in control (DMSO) and 1 μmol/L of AraC-treated cells following 1 day of treatment, in cells from patient 1. Numbers and horizontal bars indicate mean values. **, $P < 0.01$ via nonparametric Mann–Whitney *U* test. ns, not significant.

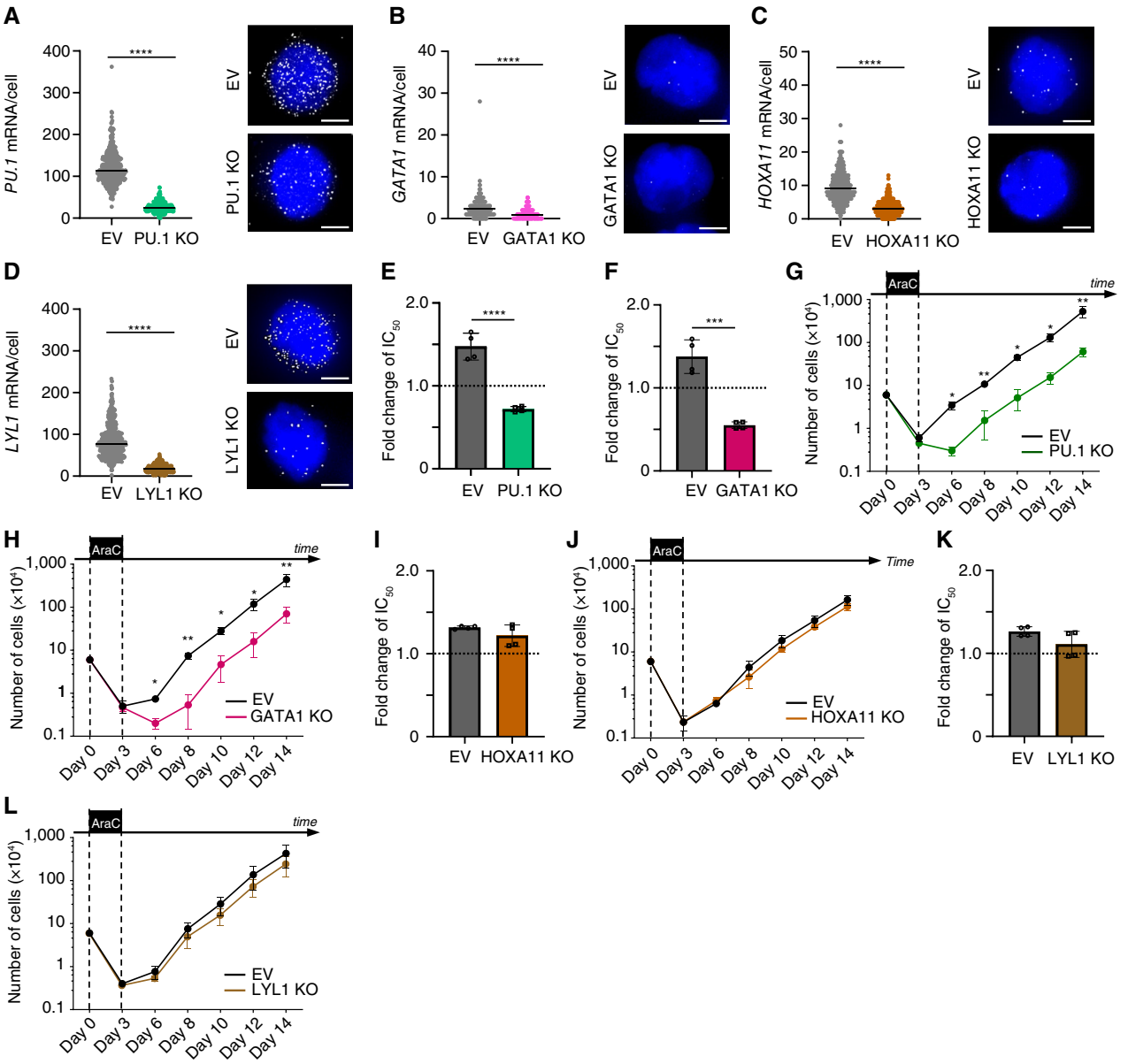

Figure 6. "AraC response" TFs are involved in the acquisition of AraC resistance. **A,** Violin plots depicting mRNA counts per cell (left) and representative smFISH images (right) for PU.1 in (empty vector-transfected) control and CRISPR-mediated PU.1 knockout HL60 cells (PU.1 KO). Horizontal bars indicate mean values. ****, $P < 0.0001$ via nonparametric Mann–Whitney *U* test. PU.1 transcripts are in white pseudocolor; DNA is in blue pseudocolor. Scale bars, 5 μm. **B,** Violin plots depicting mRNA counts per cell (left) and representative smFISH images (right) for GATA1 in (EV-transfected) control and CRISPR-mediated GATA1 knockout HL60 cells (GATA1 KO). Horizontal bars indicate mean values. ****, $P < 0.0001$ via nonparametric Mann–Whitney *U* test. GATA1 transcripts are in white pseudocolor; DNA is in blue pseudocolor. Scale bars, 5 μm. **C,** Violin plots depicting mRNA counts per cell (left) and representative smFISH images (right) for HOXA11 in control (EV-transfected) and CRISPR-mediated HOXA11 knockout HL60 cells (HOXA11 KO). Horizontal bars indicate mean values. ****, $P < 0.0001$ via nonparametric Mann–Whitney *U* test. HOXA11 transcripts are shown in white pseudocolor, and DNA is shown in blue pseudocolor. Scale bars, 5 μm. **D,** Violin plots depicting mRNA counts per cell (left) and representative smFISH images (right) for LYL1 in (EV-transfected) control and CRISPR-mediated LYL1 knockout HL60 cells (LYL1 KO). Horizontal bars indicate mean values. ****, $P < 0.0001$ via nonparametric Mann–Whitney *U* test. LYL1 transcripts are represented in white pseudocolor, and DNA is represented in blue pseudocolor. Scale bars, 5 μm. **E,** Changes in AraC sensitivity (following a 3-day treatment with 250 nmol/L of AraC) on day 14 after treatment, in control and PU.1 KO HL60 cells. The fold changes in IC_{50} values were calculated by dividing the IC_{50} of AraC-treated control and PU.1 KO cells by that of untreated control cells ($n = 4$; technical replicates). ****, $P < 0.0001$ via unpaired *t* test. **F,** Changes in AraC sensitivity (following a 3-day treatment with 250 nmol/L of AraC) on day 14 after treatment, in control and GATA1 KO HL60 cells. The fold changes in IC_{50} values were calculated by dividing the IC_{50} of AraC-treated control and GATA1 KO cells by that of untreated control cells ($n = 4$; technical replicates). ***, $P < 0.001$ via unpaired *t* test. **G,** Cell growth recovery in control and PU.1 KO HL60 cells after a 3-day AraC treatment. The y-axis represents the number of viable cells (mean ± SD) counted using trypan blue on a log scale ($n = 3$; technical replicates). *, $P < 0.05$; **, $P < 0.01$ via unpaired *t* test. **H,** Cell growth recovery in control and GATA1 KO HL60 cells after a 3-day AraC treatment. The *y*-axis represents the number of viable cells (mean ± SD) counted using trypan blue on a log scale ($n = 3$; technical replicates). *, $P < 0.05$; **, $P < 0.01$ via unpaired *t* test. **I,** Changes in AraC sensitivity (following a 3-day treatment with 250 nmol/L of AraC) on day 14 after treatment in control and HOXA11 KO HL60 cells. The fold changes in the IC_{50} values were calculated by dividing the IC_{50} of AraC-treated control and AraC-treated HOXA11 KO cells by that of the untreated control ($n = 4$; technical replicates). (*continued on following page*)

transcripts per cell (2.1, 0.1, 0.6, and 1.1 increased to 5.7, 0.2, 6.9, and 1.9 mRNA, respectively; Fig. 4G). However, interestingly, when we analyzed the changes in total nascent transcripts per TS (burst size), there were no significant changes in PU.1 and GATA1 (5.5, 6.1 to 5.6, 4.9 RNA/TS, respectively; Fig. 4H) or even slight decreases in RUNX1 and CEBPA burst size (8.5, 6 down to 6, 3.6 RNA/TS, respectively; $P < 0.0001$; Fig. 4H) after AraC treatment. This indicates that the rapid increase in ARR-TFs following AraC treatment was not caused by an increased burst size at individual TS but by an increase in burst frequency.

In contrast, when we tested four other hematopoiesis-related TFs, HOXA11, LYL1, FOXO4, and MYC, we found their mRNA expression levels to be unchanged or even slightly decreased 1 day after AraC treatment (8.7, 51, 15, and 278 mean mRNAs/cell to 8, 47, 16, and 300, respectively; Supplementary Fig. S5A and S5B). We also found no (HOXA11, LYL1, and MYC) or only a very modest (FOXO4) increase in TS burst frequency (Supplementary Fig. S5C). Likewise, the total number of nascent transcripts per cell (Supplementary Fig. S5D) and total nascent transcripts per TS (Supplementary Fig. S5E) were not or only marginally changed after AraC treatment.

To further understand the single-molecule expression dynamics of "AraC-response" TFs at the single-cell level, we simultaneously measured the expression changes of three TFs (PU.1, GATA1, and RUNX1) after 1 day of AraC treatment using multiplex smFISH. We performed t-distributed stochastic neighbor embedding (t-SNE) to visualize the differences in the expression of these TFs and identified the emergence of a unique population of cells in which the expression of all three TFs was elevated following AraC treatment (Fig. 4I and J). We tested the transcription dynamics of the same TFs in different AML cells and NB4, and again found that the "ARR-TFs" PU.1, GATA1, RUNX1, and CEBPA were consistently activated following AraC treatment, whereas the other four TFs (HOXA11, LYL1, FOXO4, and MYC) were not (Supplementary Fig. S6A–S6J). Additionally, t-SNE visualization revealed that a cell population with a high expression of all three TFs, PU.1, GATA1, and RUNX1, emerged after 1 day of AraC treatment (Supplementary Fig. S6K and S6L), suggesting that these master TFs might play a pivotal role in rapid transcription dynamics after AraC treatment.

To obtain further insight, we performed Assay for Transposase-Accessible Chromatin using sequencing (ATAC-seq) on days 0, 1, and 14 after AraC treatment in HL60 cells (Supplementary Fig. S7). HL60 cells were treated with 250 nmol/L of AraC for 1 day (day 1 cells) and for 3 days followed by culturing in control media for another 11 days (day 14 cells). Given the global mRNA induction observed upon short-term AraC treatment, we hypothesized that AraC triggers a widespread increase in promoter accessibility. However, TSS-centered heatmaps and profile plots (Supplementary Fig. S7A) revealed no significant global shifts in promoter accessibility across the three time points. Next, we focused on the accessibility of specific TF targets. In samples collected on days 1 and 14, the volcano plots (Supplementary Fig. S7B) showed that although the majority of PU.1 and GATA1 target sites remained stable, there was a visible, albeit modest, skewing toward "opening" (increased accessibility) rather than "closing," although this was not shown to be statistically significant. This trend was further supported by GSEA on day 1 (Supplementary Fig. S7C), which showed positive enrichment scores for both PU.1 and GATA1 targets, correlating with "opening" chromatin regions. Despite these subtle trends, the magnitude of chromatin remodeling did not seem to match the robust transcriptional shifts observed in the single-molecule mRNA data. These data suggest that the drug resistance phenotype is primarily driven by transcriptional reprogramming rather than broad chromatin-mediated changes.

Transcription Dynamics Following AraC Treatment in Primary AML Samples

Afterward, we investigated transcription dynamics following AraC treatment in Lin-CD34$^+$ hematopoietic stem and progenitor cells (HSPC) from 12 primary AML patient samples. Notably, HSPCs from AML samples showed modest yet significant RNA induction immediately after 1 day of 1 μmol/L AraC treatment (Fig. 5A and B; Supplementary Fig. S8A).

We also assessed the single-molecule transcription dynamics of ARR-TFs using smFISH in primary patient samples. After 1 day of 1 μmol/L AraC treatment, mature mRNA levels of PU.1, GATA1, RUNX1, and CEBPA were significantly elevated in AraC-treated primary AML samples (patients #1–5; Fig. 5C–G). We also observed a significant increase in TS burst frequency for PU.1, GATA1, and RUNX1 (3.5%, 1.4%, and 2.3% of cells with active TS bursting sites increased to 7.1%, 4.2%, and 5.4%, respectively; Fig. 5H) and the total nascent transcripts per cell (0.2, 0.06, and 0.07 increased to 0.4, 0.16, and 0.21 mRNA, respectively; Fig. 5I) in patient #1. The total nascent transcripts per TS showed no significant changes for either of the four TFs after AraC treatment in patient#1 (Fig. 5J), recapitulating our findings in AML cell lines.

ARR-TFs are Functionally Relevant for the Acquisition of AraC Resistance

As the analyses of transcriptional dynamics showed that key TFs were rapidly induced by AraC, we hypothesized that these specific TFs were functionally relevant for the acquisition of rapid resistance. To test this hypothesis, we selected two ARR-TFs, PU.1 and GATA1, and two control TFs that

Figure 6. ***(Continued)*** **J,** Cell growth recovery in control and HOXA11 KO HL60 cells after 3 days of AraC treatment. The y-axis represents the number of viable cells (mean ± SD) counted using trypan blue on a log scale ($n = 3$; technical replicates). **K,** Changes in AraC sensitivity (following a 3-day treatment with 250 nmol/L of AraC) on day 14 after treatment in control and LYL1 KO HL60 cells. The fold changes in the IC_{50} values were calculated by dividing the IC_{50} of AraC-treated control and AraC-treated LYL1 KO cells by that of untreated controls ($n = 4$; technical replicates). **L,** Cell growth recovery in control and LYL1 KO HL60 cells after 3 days of AraC treatment. The y-axis represents the number of viable cells (mean ± SD) counted using trypan blue on a log scale ($n = 3$; technical replicates). EV, empty vector.

were not altered following AraC treatment, HOXA11 and LYL1, and performed CRISPR-Cas9–mediated knockout in HL60 cells. CRISPR-Cas9 led to a reduction of PU.1, GATA1, HOXA11, and LYL1 mRNA molecules per cell of 78.2%, 58.8%, 63.3%, and 78.1%, respectively, compared with the controls (Fig. 6A–D). To begin with, there was no significant difference in cell growth between CRISPR-mediated knockout and control cells in the steady state (Supplementary Fig. S9A–S9D).

However, when we treated control and PU.1- or GATA1-targeted cells with 250 nmol/L of AraC for 3 days and assessed AraC sensitivity on day 14, PU.1- or GATA1-targeted cells showed a significant reduction in IC_{50} compared with controls (51% and 60% reduction, respectively; Fig. 6E and F). We also observed significantly greater suppression of cell proliferation and slower recovery in PU.1- and GATA1-targeted cells following AraC treatment (Fig. 6G and H). In contrast, HOXA11- and LYL1-targeted cells did not show significant differences in AraC sensitivity and cell growth kinetics compared with controls (Fig. 6I–L). Taken together, these data show that the rapid transcription dynamics of ARR-TFs are functionally important in the rapid and early acquisition of AraC resistance.

DISCUSSION

In this study, we provide evidence that the rapid increase in RNA transcription dynamics following short-term AraC treatment plays a critical role in the early and subsequent stable acquisition of AraC resistance in AML cells. Importantly, suppressing this RNA induction, particularly by targeting mRNAs encoding master TFs essential for hematopoiesis, termed ARR-TFs, effectively prevented the development of AraC resistance *in vitro*. These findings highlight rapid transcriptional dynamics as a nongenetic adaptive molecular mechanism contributing to the early acquisition of chemoresistance in AML and propose a therapeutic strategy centered on restoring proper transcriptional dynamics and regulatory machinery in leukemia and possibly other cancers.

Historically, research on chemotherapy resistance has primarily focused on identifying genetic alterations and Darwinian selection of preexisting clones responsible for resistance (19, 28–32), with current studies also uncovering epigenetic mechanisms, such as enhancer remodeling (33, 34). However, most of these studies have largely relied on highly chemoresistant cells established through prolonged drug exposure with dose escalation, which often harbor numerous genetic abnormalities. In contrast, early-stage resistance mechanisms, particularly after short-term drug treatment, remain poorly understood, with existing studies primarily focusing on newly developed targeted therapies (35, 36). This knowledge gap underscores the need for further investigation into nongenetic mechanisms that drive early-stage resistance after conventional chemotherapy, as these mechanisms may act as a prelude to more long-term and stable mechanisms such as genetic changes (37). Our study shows that rapid adaptive transcriptional induction within the first few hours of chemotherapy exposure plays an important alternative role in the acquisition of chemotherapeutic resistance. In our short-term exposure experiments using AML cell lines, we could not detect the emergence or selection of genetically defined subclones. Our data demonstrate that the observed resistance phenotype is functionally dependent on rapid transcriptional activation, which can be pharmacologically suppressed. Future studies involving advanced lineage tracing and live single-cell analysis of transcriptional induction will be necessary to reveal the exact relative contributions of selection and adaptation; of note, these possibilities are not mutually exclusive and likely both play important roles.

We observed that the population of cells with increased RNA synthesis following short-term AraC treatment exhibited greater AraC resistance than the remaining cells. As AraC is a pyrimidine nucleoside analog that primarily targets proliferative S-phase cells, its treatment results in the relative enrichment of G_1-phase cells (38, 39). Notably, some AraC-treated G_1-phase cells exhibited elevated RNA synthesis, suggesting that they were poised for G_1–S progression and subsequent proliferation—and concurrently displayed reduced sensitivity to AraC. Traditionally, chemoresistant cancer cells have been thought to originate predominantly from quiescent or dormant noncycling cells (40). However, studies have revealed that chemoresistant cells can also emerge from actively cycling (nonquiescent) populations (41, 42). For instance, G_1-phase cells with intermediate and high p21 expression during the 2-day doxorubicin treatment exhibit distinct posttreatment fates, indicating the importance of intratumoral transcriptional heterogeneity in determining treatment outcomes (42). These observations reinforce the need to explore the underappreciated role of transcription dynamics in shaping drug sensitivity shortly after treatment, which may also be a useful predictor of subsequent resistance acquisition during therapy. Further studies of transcription dynamics (e.g., PRO-Seq and DRB release assays) could be instrumental in clarifying how and where the specific transcriptional processing changes happen and dictate RNA abundance in resistant AML cells. We also propose to adopt a technique developed by our group, CLICK-CUT&Tag (43), utilizing a chemically modified AraC to investigate whether AraC interacts with the transcriptome and chromatin to regulate cellular responses in a cell context–specific manner. Furthermore, single-molecule TF chromatin residence analysis in live cells could provide insights into short-lived changes in TF function induced by AraC. Moreover, techniques such as CUT&Tag or ChIP for phospho-Ser5 RNA Pol II, combined with 3D chromatin contact analyses (e.g., Micro-C), could be instrumental in understanding the precise dynamic relationship between AraC, chromatin, and transcriptional regulation in patients with AML. Overall, our study uncovers an effect of AraC not previously described, to the best of our knowledge, and opens new avenues for the study of rapid adaptive chemotherapy resistance mechanisms that may lead to novel strategies for targeted therapeutic intervention.

Given the profound impact of transcriptional variability on cell fate decisions, targeting transcriptional dynamics holds considerable potential for unraveling developmental mechanisms and developing novel therapeutic strategies. For example, in the context of stem cell differentiation, IdU (a thymidine analog) has been shown to enhance transcriptional

noise in mouse embryonic stem cells, promoting both differentiation and reprogramming (44, 45). Similarly, loss of KAT2A, which stabilizes transcriptional noise, enhances leukemia differentiation and depletes leukemia stem-like cells in AML mouse models (13, 46). Transcriptional changes in AraC-treated AML cells (e.g., signatures associated with high oxidative phosphorylation status) have been reported previously, albeit at later time points (>1 week after AraC treatment), through comprehensive gene expression profiling, and these seemed at least in part to be associated with the acquisition of AraC resistance (47–49). Of note, to the best of our knowledge, our study provides for the first time evidence of very rapid (within 1 day) transcriptional induction and increased transcriptional heterogeneity and TF expression after AraC treatment. This increase in heterogeneity led to the emergence of a subpopulation with increased allelic bursting of ARR-TFs, which was targetable through inhibition of RNA Pol II–mediated mRNA synthesis. Hence, our study established a direct link between rapid adaptive chemotherapy resistance and transcriptional heterogeneity. Our future studies aim to further dissect this phenomenon using single-molecule approaches and fate tracking in live cells.

The dBET6 is a potent inhibitor of mRNA transcription that degrades BRD4 and blocks the assembly of the RNA Pol II elongation complex (23). Its antineoplastic effects in conjunction with other chemotherapy drugs, including AraC, have been reported (50). In this study, the combination of AraC and dBET6 activated apoptosis as an endpoint effect. Our work demonstrates that preemptive dBET6 treatment can prevent resistance in the first place in AML cell lines and patient-derived xenograft (PDX) models. dBET6 treatment prior to AraC exposure was essential to suppress the early RNA induction responsible for the subsequent acquisition of stable resistance. However, the presented work remains a preclinical proof-of-concept study that needs to be further evaluated in translational and clinical settings in the future. It is also important to note that dBET6 (23, 24, 51) has not yet been clinically approved due to toxicity, a narrow therapeutic window, and poor drug delivery (52). One potential strategy to overcome these challenges could be the development of targeted drug delivery systems, such as antibody–drug conjugates, which could precisely deliver transcription inhibitors (e.g., BET degraders) to cancer cells while minimizing on-target toxicity (53). Further research is needed to develop both the therapies targeting transcription dynamics and innovative delivery platforms to enable their safe and effective clinical application.

Finally, our study identified a subset of TFs in which transcriptional activity increased in a distinct population after just 1 day of AraC treatment, indicating their role as "AraC response" TFs crucial for early-stage resistance acquisition. Although the impact of dysregulated TF networks on chemoresistance remains relatively unexplored, MYC has been implicated in altering chemosensitivity by inducing a diapause-like state upon MYC suppression in several cancers (54, 55). Interestingly, MYC did not emerge as an AraC response TF in our study, possibly because we focused on actively cycling G_1-phase cells rather than quiescent populations.

As the role of the transcription dynamics of specific TFs in modulating chemosensitivity becomes clearer, there may also be opportunities to develop TF-targeted therapies to prevent chemoresistance. Although significant challenges persist in general in the therapeutic targeting of TFs, advances—including the development of small molecules that modulate PU.1 transcription dynamics and its transcriptional network (43)—highlight the fundamental feasibility of such approaches. Thus, detailed mapping of TF dynamics using high-resolution techniques and their dysregulation during resistance acquisition may ultimately lead to novel TF-targeted therapies for AML and other diseases driven by aberrant transcriptional programs. Finally, our study also opens the possibility of future studies of transcriptional induction mechanisms in nongenetic chemoresistance and their applicability in other tumor types.

METHODS

Compounds and Cells

AraC (MedChem, HY-13605), ActD (Sigma, A9415), dBET6 (MedChem, HY-112588), CX-5461 dihydrochloride (CX5461; MedChem, HY-13323A), and ellipticine (MedChem, HY-15753) were purchased from either Sigma or MedChemExpress. AraC, ActD, dBET6, and ellipticine were dissolved in DMSO, and CX5461 was dissolved in water.

HL60 (ATCC, CCL-240), NB4 (DSMZ no. ACC207), and MOLM14 (DSMZ no. ACC777) cells were originally purchased from the ATCC or DSMZ and cultured in complete media [RPMI 1640 medium (Corning, 10-040-CV) supplemented with 10% heat-inactivated FBS (Gemini, 900-108) and 1% penicillin–streptomycin (PS; Corning, 30-002-CI)]. All cells were maintained in an incubator at 37°C and 5% CO_2 under the conditions with no contamination from *Mycoplasma*.

All key reagents, including drugs, cells, antibodies, and software, are listed with RRIDs in the Key Resource Table (Supplementary Table S1).

AraC Treatment

HL60, NB4, and MOLM14 were treated with an IC_{95} dose of AraC, which was 250 nmol/L for HL60 and 500 nmol/L for NB4 and MOLM14. The duration of single treatments for short-term exposure experiments was 1 day, while it was 3 days for some of the longer-term experiments. The control cells were treated with DMSO for the same durations. After treatment, the cells were washed in complete media and then cultured for additional days to assess the changes in AraC sensitivity at day 14 or 28. For ATAC-seq experiments, the cells were harvested at days 0, 1, and 14 (3-day pretreated) for chromatin extraction and analysis.

Cell Viability Assay

Cell viability was determined using the CellTiter-Blue Cell Viability Assay (Promega, G8080) according to the manufacturer's instructions. Briefly, 5×10^3 cells were plated in each well of a 96-well plate containing media with a serial dilution of AraC. The plates were incubated for 72 hours at 37°C, 5% CO_2. Twenty microliters of CellTiter-Blue reagent was added to each well. The plates were then incubated for a further 2 hours and read using a VICTOR X5 multilabel plate reader (PerkinElmer). The IC_{50} value was determined using GraphPad Prism software (version 8.4.3; GraphPad Software) by fitting the data to the nonlinear regression "log (inhibitor) versus normalized response."

Nascent RNA Labeling by EU

Nascent RNA synthesis activity was detected using an RNA Synthesis Assay Kit (Abcam, ab228561) according to the manufacturer's instructions. Briefly, cells were cultured in complete media and

pulsed for 1 hour with EU at a final concentration of 1 mmol/L before fixation with fixative solution for 15 minutes. After fixation, the cells were permeabilized with permeabilization buffer for 10 minutes and washed with Wash Buffer IV. The samples were incubated with the click reaction mixture for 30 minutes at room temperature in the dark. The reaction mixture was then removed, and the samples were washed once with Wash Buffer IV, followed by a 1× PBS wash. The samples were then stained with DAPI (Millipore, 10236276001) and analyzed using an FACSymphony A5 flow cytometer (BD Biosciences). Flow cytometry data were analyzed using FACSDiva and FlowJo software (BD Biosciences).

RNA and Cell-Cycle Assay by Pyronin Y

The RNA expression level was detected using a cell-cycle assay in live cells using pyronin Y (Sigma, P9172) and Hoechst 33342 (Invitrogen, H3570) as previously described (56). Briefly, the cells were first stained with Hoechst 33342 (10 μg/mL) at 37°C for 45 minutes in freshly prepared Hoechst staining medium (RPMI 1640 + 10% FBS + PS + 20 mmol/L of HEPES + 50 μg/mL of Verapamil) before pyronin Y (5 μg/mL) was added and the cells were stained for another 15 minutes. The cells were then washed once and analyzed using a FACSymphony A5 flow cytometer or sorted into PY^{High} and PY^{Low} cells in the G_0–G_1 cell-cycle phase using a FACSAria III cell sorter (BD Biosciences).

RNA Expression Detection Assay by SYTO RNASelect Dye

The total RNA expression levels were detected using SYTO RNASelect dye (Invitrogen, S32703) with Hoechst in live cells, according to the manufacturer's instructions. Briefly, the cells were first stained with Hoechst 33342 (10 μg/mL) at 37°C for 45 minutes in cell culture media before 10 mmol/L of SYTO RNASelect dye was added, and the cells were stained for another 30 minutes. The cells were then washed once in 1× PBS and analyzed using an FACSymphony A5 flow cytometer.

WES

For WES, the genomic DNA was isolated using the QIAamp DNA Mini Kit (QIAGEN, 51304). The quantity and quality of the isolated DNA were assessed using a NanoDrop 2000 spectrophotometer (Thermo Fisher Scientific). Library preparation and sequencing were performed by Novogene Co., Ltd. Briefly, sequencing libraries were generated using an Agilent SureSelect Human All Exon Kit V6 (Agilent Technologies, 5190-8864). Then, 150-bp paired-end sequencing was performed on the Illumina NovaSeq platform (Illumina) using the constructed DNA libraries for WES. The untreated cells were used as controls. Raw sequencing reads (FASTQ files) were first assessed for quality using FastQC (version 0.12.1). Adapter sequences and low-quality bases were trimmed using Cutadapt (version 3.5) with the removal of the Illumina adapter sequence (AGATCGGAAGAGC), a minimum read length of 30 bp, a quality trimming threshold of Q20, and the removal of terminal ambiguous bases. Trimmed reads were aligned to the human reference genome (GRCh38 primary assembly) using BWA-MEM (version 0.7.17). PCR duplicates were marked using GATK MarkDuplicates (version 4.6.2). For small variant calling, SNVs and small InDels were identified using GATK (version 4.6.2). Variant calling was performed using HaplotypeCaller in GVCF mode for each sample. Individual GVCFs were combined using CombineGVCFs, followed by joint genotyping with GenotypeGVCFs to generate a multisample VCF file. Structural variants were identified using Manta (version 1.6.0). Deduplicated BAM files were used as input, and structural variant discovery was performed using the GRCh38 reference genome. SNVs were detected using MuTect (57), and InDels were identified by Strelka (58). The detected SNVs and InDels are summarized in Supplementary Table S2.

qRT-PCR and RNA-Seq

The RNA was extracted from cells using an RNeasy Mini Kit (QIAGEN, 74004), and for qRT-PCR, reverse transcription of RNA (1 μg) was performed using SuperScript II Reverse Transcriptase (Bio-Rad, 1708890). qPCR was performed on a ViiA7 instrument using the Power SYBR Green PCR Master Mix (Thermo Fisher, 4368577). Expression levels were normalized to GAPDH, and the primers used are listed in Supplementary Table S3. For mRNA-seq, library preparation and transcriptome sequencing were performed by Novogene Co., Ltd. Briefly, RNA quantity and quality were assessed using a NanoDrop 2000 (Thermo Fisher) and a Bioanalyzer (Agilent Technologies), respectively. The total RNA (400 ng of total RNA each from control and AraC-treated cells or PY^{High} and PY^{Low} cells) was enriched using poly T oligo–attached magnetic beads, fragmented, and reverse-transcribed into cDNA. Three technical replicates for each sample were used for further cDNA library preparation. cDNA libraries were constructed and sequenced on an Illumina NovaSeq platform to generate paired-end reads. Raw sequencing reads (FASTQ files) were first assessed for quality using FastQC (version 0.12.1). Adapter sequences and low-quality bases were trimmed using Cutadapt (version 3.5) with the removal of the Illumina adapter sequence (AGATCGGAAGAGC), a minimum read length of 30 bp, a quality trimming threshold of Q20, and the removal of terminal ambiguous bases. Trimmed reads were aligned to the human reference genome (GRCh38 primary assembly) using STAR (version 2.7.10a) in the two-pass mode to improve splice junction detection. Alignments were generated as coordinate-sorted BAM files. Gene-level counts were obtained using featureCounts (Subread version 2.0.1) with the corresponding GTF file annotation (e.g., GENCODE version 44). FeatureCounts was run in paired-end mode with strand specificity set to reverse-stranded. Differential gene expression analysis was performed using DESeq2 (version 1.46.0) in R (version 4.4.2). Raw count matrices were imported into DESeq2 and normalized using the median-of-ratios method to account for sequencing depth and RNA composition differences. Differential expression was calculated using the negative binomial generalized linear model framework implemented in DESeq2.

GSEA

GSEA was performed using the fgsea package (version 1.32.4) in R. Genes were ranked by $\log_2$ fold change from DESeq2 differential expression results. Gene sets were obtained from MSigDB using the msigdbr package (version 25.1.1). Preranked GSEA was performed using normalized enrichment scores, and pathways with an adjusted *P* value (Benjamini–Hochberg) <0.1 were considered significant. The gene sets used are listed in Supplementary Table S4.

scRNA-seq

The scRNA-seq libraries were generated using the 10x Genomics Chromium Single Cell 3′ version 3 platform. Sequencing data were processed using Cell Ranger (version 7.0.1) with the GRCh38-3.0.0 human reference transcriptome (refdata-cellranger-GRCh38-3.0.0). Intronic reads were included during alignment and quantification. After quality filtering (>500 and <7,000 genes per cell; <20% mitochondrial reads), per-cell gene and Unique Molecular Identifier (UMI) counts were extracted and compared between PY-high and PY-low samples.

ATAC-Seq

Raw sequencing reads (FASTQ files) were first assessed for quality using FastQC (version 0.12.1). Adapter sequences and low-quality bases were trimmed using Cutadapt (version 3.5) with the removal of the Nextera transposase sequence (CTGTCTCTTATACACATCT), a minimum read length of 30 bp, a quality trimming threshold of Q20, and the removal of terminal ambiguous bases. Paired-end reads were aligned to the human reference genome (GRCh38) using Bowtie2

(version 2.2.5) with the very sensitive preset, a maximum fragment length of 2,000 bp (–X 2000), and discordant and mixed alignments disabled. The alignments were converted into BAM format using SAMtools. Mitochondrial reads were removed using SAMtools, and PCR duplicates were removed using Picard MarkDuplicates. BAM files were indexed after each processing step. To correct for Tn5 transposase insertion bias, read start sites were shifted (+4 bp for positive-strand reads and –5 bp for negative-strand reads). Only reads with adjusted coordinates ≥1 were retained. The shifted BAM files were sorted and indexed using SAMtools. The peaks were called using MACS2 with paired-end mode, human genome size (–g hs), duplicate retention enabled, and summit calling activated (–call-summits). Peaks identified in individual samples (MACS2 narrowPeak files) were concatenated and merged using BEDTools to generate a consensus peak set. Peak summits were centered and extended ±250 bp to create fixed-width 500-bp regions. The overlapping regions were remerged to avoid redundancy. Regions overlapping ENCODE hg38 blacklist loci were removed using BEDTools intersect. The final filtered peak set was sorted and used as a consensus reference. Read counts per peak were quantified using BEDTools coverage in sorted mode, with genome size information provided (–g hg38.genome). Raw fragment counts per region were extracted for downstream normalization and differential accessibility analyses. Raw fragment counts per consensus peak were assembled into a count matrix across all samples. Peaks were annotated using genomic coordinates, and differential accessibility analysis was performed in R using DESeq2. Peaks with fewer than 10 total counts across all samples were excluded prior to analysis.

smFISH

To design mRNA-specific probes for sequential smFISH, the full-length transcript of each gene was used as input for PaintSHOP (https://paintshop.io/; ref. 59) to retrieve 10 to 29 primary targeting sequences (23–39 bp), separated by at least 10 bp. Putative sequences were screened for off-target activity using NCBI Blast (https://blast.ncbi.nlm.nih.gov/Blast.cgi). The selected sequences were then concatenated at both the 5′- and 3′-ends, flanking the same readout 20mer sequences (RO-1: ATACTGGAGCGACGCGTGAT, RO-2: GTTTGAAGATTCGACCTGGA, RO-4: CTAAGGTACCTAATTG CCTAG, or RO-6: GTACCGTAGGATCTGATGAA), generating a final "primary probe" (Supplementary Table S5). The smFISH immunofluorescence staining procedure and analysis were performed as described previously (9, 43). Briefly, untreated control and AraC-treated HL60 (250 μmol/L for 1 day) or NB4 cells (500 μmol/L for 1 day) were attached to coverslips using poly-L-lysine coating (Sigma-Aldrich). The residual medium was washed with PBS, and cells were fixed in 3.2% paraformaldehyde (PFA; Electron Microscopy Sciences), diluted in PBS with 1 mmol/L of $MgCl_2$ (PBSM), for 10 minutes at room temperature. The cells were then permeabilized in 0.1% Triton X-100 in PBSM for 10 minutes. After washing with PBSM, the cells were incubated at room temperature with 30% prehybridization buffer [30% formamide, 2× saline-sodium citrate (SSC) buffer] for 10 minutes. Primary hybridization was done in a 30% hybridization buffer consisting of 10% dextran sulfate, 30% formamide, 2× SSC, 2 mmol/L of vanadyl-ribonucleoside complex (VRC), 10 mg/mL of sheared ssDNA from salmon sperm, 10 mg/mL of *E. coli* tRNA, 10 mg/mL of molecular grade bovine serum albumin (BSA), and 100 ng of primary probe mixes, overnight at 37°C. Thereafter, the cells were washed twice with 30% prehybridization buffer for 15 minutes at 37°C and twice with 2× SSC. They were then postfixed in 3.2% PFA in PBSM for 10 minutes, followed by washing in 2× SSC. Primary stained cells were incubated with 10% prehybridization buffer (10% formamide, 2× SSC) for 10 minutes at 37°C and stained with 10% dextran sulfate, 10% formamide, 2× SSC, 2 mmol/L of VRC, 10 mg/mL of sheared ssDNA from salmon sperm, 10 mg/mL of *E. coli* tRNA, 10 mg/mL of BSA, and 10 ng of Cy3-, Cy5-, AF488-, or AF594-coupled "secondary readout probe" (Supplementary Table S5) for each gene for 4 hours at 37°C. The cells were then washed twice for 10 minutes in 10% prehybridization buffer, followed by a final wash in 2× SSC. They were then mounted in ProLong Diamond Antifade reagent plus 4′,6-diamidino-2-phenylindole (DAPI; Invitrogen, P36935). Images were acquired using an oil immersion 100× objective on a Leica Thunder fluorescence microscope (Leica) or a Nikon Ti2-E fluorescence microscope (Nikon). The exposure times were 250, 300, 250, 300, and 10 milliseconds for Cy3, Cy5, AF488, AF594, and DAPI, respectively. Z stacks spanning the entire volume of the cells were acquired by imaging every 300 nm along the z-axis. For data analysis, single-molecule mRNA and TS detection was performed using freely available MATLAB-written software FISH-quant (60), via 3D Gaussian fitting of thresholded spots, implemented in MATLAB R2021a. smFISH was performed on three biological replicates in each experiment. Data from these independent experiments were then pulled together, and statistical significance was derived from the Mann–Whitney *U* test to analyze the true shift in mean on a per-cell basis.

t-SNE Analysis

The t-SNE analysis was performed on multiplex smFISH data using MATLAB with the "tsne" function. The expression levels of PU.1, GATA1, and RUNX1 were extracted from the smFISH dataset obtained simultaneously in different fluorescent dyes (Cy3 for PU.1, AF594 for GATA1, and Cy5 for RUNX1) and used as input for t-SNE. The data were reduced to two dimensions with a perplexity of 20. The resulting t-SNE coordinates were combined with the original dataset and visualized using scatter plots.

Generation of CRISPR-Cas9–Mediated TF Knockout Cells

Gene editing was performed using the CRISPR-Cas9 technique as described previously (61). Briefly, three target-specific oligonucleotides were designed to knockout PU.1, GATA1, HOXA11, and LYL1, respectively (Supplementary Table S3), using a bioinformatics tool, CHOPCHOP (https://chopchop.cbu.uib.no/; ref. 62), and were inserted into the CRISPR-Cas9 genome-editing vector [pSpCas9(BB)-2A-GFP (PX458), plasmid ID: 48138; Addgene]. These three target-specific vectors were transfected into HL60 cells with the nucleofector system (Lonza). After GFP sorting, which limits dilution, and genotype screening (Supplementary Table S3), sublines for each TF were established. The sublines were screened using RT-qPCR (Supplementary Table S3) and smFISH. The control sublines were obtained using the same protocol using vectors without target-specific oligonucleotides.

Monitoring Cell Growth Recovery after AraC Treatment

To assess the differences in cell growth recovery dynamics following AraC treatment, CRISPR-Cas9–mediated TF-knockout cells and control cells were plated in triplicate wells (30,000 cells per well) in 1 mL of complete medium (RPMI-1640 with 10% FBS and 1% PenStrep) in the 24-well plates. Both cell types were treated with 250 nmol/L of AraC for 3 days. After AraC withdrawal, the cells were cultured in AraC-free medium, with an equal number of cells in each well on days 6, 8, 10, and 12. Cell growth was monitored by counting viable cells using a hemocytometer with trypan blue (Thermo Fisher, 15250061) staining on days 3, 6, 8, 10, 12, and 14.

Mice

NSG mice were purchased from The Jackson Laboratory (Stock #005557). The mice were maintained in our animal facility under specific pathogen-free conditions, and all experiments were approved by the Albert Einstein College of Medicine Institutional Animal Care and Use Committee (protocol 0000-1099).

Murine Subcutaneous Tumor Model

For subcutaneous transplantation, HL60 and NB4 cells were harvested to a concentration of 5×10^6 and 1×10^7, respectively, washed and resuspended in PBS, and mixed 1:1 with 75 μL of Matrigel (Corning, CLS356234-1EA) on ice. The 150 μL of cell suspension was injected into the shaved subcutaneous flank of NSG mice without irradiation conditioning. After 4 days of tumor growth, dBET6 (150 μg/tumor/day for HL60 and 50 μg/tumor/day for NB4, days 1–6), AraC (2 mg/tumor/day for HL60 and 3 mg/tumor/day for NB4, days 4–6), or both (n = 7–8 for each condition) were directly administered to the tumors by subcutaneous injection. Tumors were measured every 2 days by placing a digital caliper on the skin and measuring the longest diameter (l), shortest diameter (s), and height (h). The tumor volume was calculated as ($l \times s \times h \times 0.52$; ref. 63) until the tumor volumes approached the Institutional Animal Care and Use Committee–approved limits. Animals were sacrificed by CO_2 asphyxiation, followed by cervical dislocation. For tumor cell analysis, tumors were excised on day 6 and subjected to flow cytometry experiments for RNA expression analysis. In flow cytometry analysis, tumor cells were stained with pyronin Y (#P9172, Sigma), Hoechst 33342 (#H3570, Invitrogen), and human CD45 APC-Cy7 antibody (#304014, BioLegend) for mouse cell exclusion.

Primary AML Samples

This study was conducted in accordance with the ethical standards of the Declaration of Helsinki. Adult AML leukapheresis blood samples or bone marrow aspirates from 12 patients were obtained after written informed consent and following Albert Einstein College of Medicine Institutional Review Board approval (2005-536). For this small exploratory study, primary samples were randomly selected based on availability and without exclusion or inclusion criteria. The clinical characteristics of the primary AML samples used for experiments are listed in Supplementary Table S6. For flow cytometry experiments, 1 to 2 million cells were thawed and cultured in 1 mL of StemSpan SFEM II medium (StemCell Tech, 09605) plus 1× CC100 growth cocktail (StemCell Tech, 02690) and TPO (50 ng/mL, R&D Systems, 288-TPN) overnight. The next day, cells were treated in the presence of AraC (1 μmol/L) or DMSO for 1 day. After incubation, the cells were stained with pyronin Y (Sigma, P9172) and Hoechst 33342 (Invitrogen, H3570) in addition to the following antibodies: lineage FITC (CD3/14/16/19/20/56, BioLegend, 348801, 1:50 dilution), CD235a FITC (BD Biosciences, 559943, 1:50 dilution), and CD34 PE (BD Biosciences, 555824, 1:50 dilution) in FACS buffer (2% FBS in 1× PBS). Lineage and CD235a-negative and CD34-positive gates were used to define HSPCs in primary AML samples (Supplementary Fig. S8). Flow cytometry analysis was performed on a BD FACSymphony A5, and sorting was performed on a BD FACS Aria II. For smFISH experiments, the HSPCs of untreated and AraC-treated primary AML cells were attached to coverslips coated with 10 μg/mL of anti-CD44 biotin (BioLegend, 103004, 1:1,000 dilution; ref. 64) instead of poly-L-lysine. smFISH staining was performed as described above.

Statistical Analysis

The data are represented as either bar graphs representing means and SDs or violin dot plots for scRNA measurements. n represents the number of technical repeats or total cells analyzed, as explained in figure legends. Statistical comparisons between groups were performed using unpaired t tests, Mann–Whitney U nonparametric tests, or Wilcoxon sum-rank tests (scRNA-seq data). All experiments were performed with a minimum of two or three technical replicates. A P value <0.05 was used to demonstrate whether a significant difference was present between the compared groups. A P value >0.05 was denoted as nonsignificant. All the flow cytometry data were analyzed using FlowJo software.

Data Availability

Raw sequencing data for WES, bulk RNA-seq, scRNA-seq, and ATAC-seq are available on the NCBI Gene Expression Omnibus (ncbi.nlm.nih.gov/geo/) under the accession numbers PRJNA1433834, GSE324057, GSE324170, and GSE324058.

Authors' Disclosures

G. Tatsumi reports grants from JSPS Overseas Research Fellowships during the conduct of the study. A. Verma reports research funding from Bristol Myers Squibb, Janssen, MedPacto, Curis, Prelude, Halia, and Ryvu; compensation as a scientific advisor to Stelexis BioSciences, Halia, Calico, and Aurigene; and equity ownership in Roshon, Stelexis, and clinStreet. U. Steidl reports grants from NIH/NCI and the V Foundation during the conduct of the study, as well as personal fees and equity ownership in Stelexis BioSciences and equity ownership in Roshon Therapeutics outside the submitted work. No disclosures were reported by the other authors.

Authors' Contributions

G. Tatsumi: Conceptualization, formal analysis, investigation, methodology, writing–original draft. **R. Kumari:** Formal analysis, investigation, methodology, writing–review and editing. **Y. Suzuki:** Investigation. **S. Li:** Formal analysis, investigation. **R. Scharf:** Formal analysis, investigation. **S.J. Taylor:** Investigation. **S. Sundaravel:** Investigation. **A. Verma:** Resources, supervision. **J.C. Wheat:** Formal analysis, methodology. **U. Steidl:** Conceptualization, resources, data curation, supervision, funding acquisition, writing–review and editing.

Acknowledgments

We thank the Einstein Analytical Imaging Facility (NIH P30CA013330) and Flow Cytometry Core Facility, as well as the Stem Cell Isolation and Xenotransplantation Core Facility (funded by NYSTEM grant #C029154) of the Ruth L. and David S. Gottesman Institute for Stem Cell Research and Regenerative Medicine for expert services and support. This work was supported by NIH grant R35CA253127 and V Foundation Grant AST2025-007 (to U. Steidl), and G. Tatsumi was supported by a Japan Society for the Promotion of Science overseas research fellowship. R. Kumari was supported by a Career Development Fellowship from Blood Cancer United. S.J. Taylor was supported by a Young Investigator award from the Edward P. Evans Foundation. S. Sundaravel was supported by grants from the NCI (K00CA223044) and Blood Cancer United (3439-25). U. Steidl holds the Edward P. Evans Endowed Professorship in Myelodysplastic Syndromes at Albert Einstein College of Medicine. The Endowed Professorship was supported by a grant from the Edward P. Evans Foundation. This work was supported by Jane A. and Myles P. Dempsey.

Note

Supplementary data for this article are available at Blood Cancer Discovery Online (https://bloodcancerdiscov.aacrjournals.org/).

Received August 17, 2025; revised March 9, 2026; accepted May 6, 2026; posted first May 18, 2026.

REFERENCES

1. Liu H, Stanworth SJ, McPhail S, Bishton M, Rous B, Bacon A, et al. Impact of patient demographics on treatment outcomes in AML: a population-based registry in England, 2013-2020. Blood Adv 2024;8:4593–605.
2. Kantarjian H, Borthakur G, Daver N, DiNardo CD, Issa G, Jabbour E, et al. Current status and research directions in acute myeloid leukemia. Blood Cancer J 2024;14:163.
3. DeWolf S, Tallman MS. How I treat relapsed or refractory AML. Blood 2020;136:1023–32.
4. Stratmann S, Yones SA, Mayrhofer M, Norgren N, Skaftason A, Sun J, et al. Genomic characterization of relapsed acute myeloid leukemia reveals novel putative therapeutic targets. Blood Adv 2021;5:900–12.
5. Cortes JE, Kantarjian HM, Shah NP, Bixby DL, Mauro MJ, Flinn IW, et al. Ponatinib in refractory Philadelphia chromosome–positive leukemias. N Engl J Med 2012;367:2075–88.
6. Perl AE, Martinelli G, Cortés JE, Neubauer A, Berman E, Paolini S, et al. Gilteritinib or chemotherapy for relapsed or refractory FLT3ITD. N Engl J Med 2019;381:1728–40.
7. Perl AE, Altman JK, Cortes JE, Smith CC, Litzow MR, Baer MR, et al. Selective inhibition of FLT3 by Gilteritinib in relapsed or refractory acute myeloid leukaemia: a multicentre, first-in-human, open-label, phase 1 to 2 study. Lancet Oncol 2017;18:1061–75.
8. Bell CC, Fennell K, Chan Y-C, Rambow F, Yeung MM, Vassiliadis D, et al. Targeting enhancer switching overcomes non-genetic drug resistance in acute myeloid leukaemia. Nat Commun 2019;10:2723.
9. Wheat JC, Sella Y, Willcockson MA, Skoultchi AI, Bergman A, Singer RH, et al. Single-molecule imaging of transcription dynamics in somatic stem cells. Nature 2020;583:431–6.
10. Moris N, Edri S, Seyres D, Kulkarni R, Domingues AF, Balayo T, et al. Histone acetyltransferase KAT2A stabilizes pluripotency with control of transcriptional heterogeneity.Stem Cells 2018;36:1828–38.
11. Mohammed H, Hernando-Herraez I, Savino A, Scialdone A, Macaulay IC, Mulas C, et al. Single-cell landscape of transcriptional heterogeneity and cell fate decisions during mouse early gastrulation. Cell Rep 2017;20:1215–28.
12. Jiménez S, Schreiber V, Mercier R, Gradwohl G, Molina N. Characterization of cell-fate decision landscapes by estimating transcription factor dynamics. Cell Rep Methods 2023;3:100512.
13. Gupta S, Dovey OM, Domingues AF, Cyran OW, Cash CM, Giotopoulos G, et al. Transcriptional variability accelerates preleukemia by cell diversification and perturbation of protein synthesis. Sci Adv 2022;8:eabn4886.
14. Zhang J, Han X, Ma L, Xu S, Lin Y. Deciphering a global source of non-genetic heterogeneity in cancer cells. Nucleic Acids Res 2023;51:9019–38.
15. Goyal Y, Busch GT, Pillai M, Li J, Boe RH, Grody EI, et al. Diverse clonal fates emerge upon drug treatment of homogeneous cancer cells. Nature 2023;620:651–9.
16. Emert B, Cote C, Torre EA, Dardani I, Jiang C, Jain NK, et al. Variability within rare cell states enables multiple paths toward drug resistance. Nat Biotechnol 2021;39:865–76.
17. Shaffer SM, Emert BL, Reyes Hueros RA, Cote C, Harmange G, Schaff DL, et al. Memory sequencing reveals heritable single-cell gene expression programs associated with distinct cellular behaviors. Cell 2020;182:947–59.e17.
18. Hiddemann W. Cytosine arabinoside in the treatment of acute myeloid leukemia: the role and place of high-dose regimens. Ann Hematol 1991;62:119–28.
19. Lamba JK. Genetic factors influencing cytarabine therapy. Pharmacogenomics 2009;10:1657–74.
20. Mesa RA, Loegering DA, Powell HL, Flatten KS, Arlander SJH, Dai NT, et al. Heat shock protein 90 inhibition sensitizes acute myelogenous leukemia cells to cytarabine. Blood 2005;106:318–27.
21. Schenk EL, Koh BD, Flatten KS, Peterson KL, Parry D, Hess AD, et al. Effects of selective checkpoint kinase 1 inhibition on cytarabine cytotoxicity in acute myelogenous leukemia cells in vitro. Clin Cancer Res 2012;18:5364–73.
22. Hagelskamp F, Borland K, Ammann G, Kaiser S. Temporal resolution of NAIL-MS of tRNA, rRNA and poly-a RNA is overcome by actinomycin D. RSC Chem Biol 2023;4:354–62.
23. Winter G, Mayer A, Buckley DL, Erb MA, Roderick JE, Vittori S, et al. BET bromodomain proteins function as master transcription elongation factors independent of CDK9 recruitment. Mol Cell 2017;67:5–18.e19.
24. Arnold M, Bressin A, Jasnovidova O, Meierhofer D, Mayer A. A BRD4-mediated elongation control point primes transcribing RNA polymerase II for 3′-processing and termination. Mol Cell 2021;81:3589–603.e13.
25. Drygin D, Lin A, Bliesath J, Ho CB, O'Brien S, Proffitt C, et al. Targeting RNA polymerase I with an oral small molecule CX-5461 inhibits ribosomal RNA synthesis and solid tumor growth. Cancer Res 2011;71:1418–30.
26. Andrews WJ, Panova T, Normand C, Gadal O, Tikhonova IG, Panov KI. Old drug, new target. J Biol Chem 2013;288:4567–82.
27. Tenen DG. Disruption of differentiation in human cancer: AML shows the way. Nat Rev Cancer 2003;3:89–101.
28. Malani D, Murumägi A, Yadav B, Kontro M, Eldfors S, Kumar A, et al. Enhanced sensitivity to glucocorticoids in cytarabine-resistant AML. Leukemia 2016;31:1187–95.
29. Su Q, Huang P, Luo X, Zhang P, Li H, Chen Y. Artesunate reverses cytarabine resistance in acute myeloid leukemia by blocking the JAK/STAT3 signaling. Hematology 2023;28:2255802.
30. Wu B, Mao Z, Wang Z, Wu P, Huang H, Zhao W, et al. Deoxycytidine kinase (DCK) mutations in human acute myeloid leukemia resistant to cytarabine. Acta Haematol 2021;144:534–41.
31. Tsimberidou AM, Paterakis G, Androutsos G, Anagnostopoulos N, Galanopoulos A, Kalmantis T, et al. Evaluation of the clinical relevance of the expression and function of P-glycoprotein, multidrug resistance protein and lung resistance protein in patients with primary acute myelogenous leukemia. Leuk Res 2002;26:143–54.
32. Shlush LI, Mitchell A, Heisler L, Abelson S, Ng SWK, Trotman-Grant A, et al. Tracing the origins of relapse in acute myeloid leukaemia to stem cells. Nature 2017;547:104–8.
33. Williams MS, Amaral FMR, Simeoni F, Somervaille TCP. A stress-responsive enhancer induces dynamic drug resistance in acute myeloid leukemia. J Clin Invest 2020;130:1217–32.
34. Guo L, Li J, Zeng H, Guzman A, Li T, Lee M, et al. A combination strategy targeting enhancer plasticity exerts synergistic lethality against BETi-resistant leukemia cells. Nat Commun 2020;11:740.
35. Gebru MT, Atkinson JM, Young MM, Zhang L, Tang Z, Liu Z, et al. Glucocorticoids enhance the antileukemic activity of FLT3 inhibitors in FLT3-mutant acute myeloid leukemia. Blood 2020;136:1067–79.
36. Shaffer SM, Dunagin MC, Torborg S, Torre EA, Emert B, Krepler C, et al. Rare cell variability and drug-induced reprogramming as a mode of cancer drug resistance. Nature 2017;546:431–5.
37. Bai X, Fisher DE, Flaherty KT. Cell-state dynamics and therapeutic resistance in melanoma from the perspective of MITF and IFNγ pathways. Nat Rev Clin Oncol 2019;16:549–62.
38. Banker DE, Groudine M, Willman CL, Norwood T, Appelbaum FR. Cell cycle perturbations in acute myeloid leukemia samples following in vitro exposures to therapeutic agents. Leuk Res 1998;22:221–39.
39. Li Z, Guo J, Chen Q, Wang C-Y, Zhang W, Yao M, et al. Exploring the antitumor mechanism of high-dose cytarabine through the metabolic perturbations of ribonucleotide and deoxyribonucleotide in human promyelocytic leukemia HL-60 cells. Molecules 2017;22:499.
40. Thomas D, Majeti R. Biology and relevance of human acute myeloid leukemia stem cells. Blood 2017;129:1577–85.
41. Karigane D, Fan AC, Kayamori K, Nakauchi Y, Koehnke T, Rangavajhula AS, et al. Intra-leukemic IFNγ signaling mediates cell cycle suppression and chemoresistance in AML. Blood 2023;142(Suppl 1):406.
42. Ashraf HM, Moser J, Spencer SL. Senescence evasion in chemotherapy: a sweet spot for P21. Cell 2019;178:267–9.
43. Taylor SJ, Stauber J, Bohorquez O, Tatsumi G, Kumari R, Chakraborty J, et al. Pharmacological restriction of genomic binding sites redirects PU.1 pioneer transcription factor activity. Nat Genet 2024;56:2213–27.

44. Desai RV, Chen X, Martin B, Chaturvedi S, Hwang D-W, Li W, et al. A DNA repair pathway can regulate transcriptional noise to promote cell fate transitions. Science 1979;2021:373.
45. Khetan N, Zuckerman B, Calia GP, Chen X, Garcia Arceo X, Weinberger LS. Single-cell RNA sequencing algorithms underestimate changes in transcriptional noise compared to single-molecule RNA imaging. Cell Rep Methods 2024;4:100933.
46. Domingues AF, Kulkarni R, Giotopoulos G, Gupta S, Vinnenberg L, Arede L, et al. Loss of Kat2a enhances transcriptional noise and depletes acute myeloid leukemia stem-like cells. Elife 2020;9:e51754.
47. Farge T, Saland E, Toni Fde, Aroua N, Hosseini M, Perry R, et al. Chemotherapy-resistant human acute myeloid leukemia cells are not enriched for leukemic stem cells but require oxidative metabolism. Cancer Discov 2017;7:716–35.
48. Naldini MM, Casirati G, Barcella M, Rancoita PMV, Cosentino A, Caserta C, et al. Longitudinal single-cell profiling of chemotherapy response in acute myeloid leukemia. Nat Commun 2023;14:1285.
49. Love MI, Huber W, Anders S. Moderated estimation of fold change and dispersion for RNA-seq data with DESeq2. Genome Biol 2014;15:550.
50. Bauer K, Hauswirth A, Gleixner KV, Greiner G, Thaler J, Bettelheim P, et al. BRD4 degraders may effectively counteract therapeutic resistance of leukemic stem cells in AML and ALL. Am J Hematol Am J Hematol 2024;99:1721–31.
51. Zheng B, Gold S, Iwanaszko M, Howard BC, Wang L, Shilatifard A. Distinct layers of BRD4-PTEFb reveal bromodomain-independent function in transcriptional regulation. Mol Cell 2023;83:2896–910.e4.
52. Shorstova T, Foulkes WD, Witcher M. Achieving clinical success with BET inhibitors as anti-cancer agents. Br J Cancer 2021;124:1478–90.
53. Nakazawa Y, Miyano M, Tsukamoto S, Kogai H, Yamamoto A, Iso K, et al. Delivery of a BET protein degrader via a CEACAM6-targeted antibody-drug conjugate inhibits tumour growth in pancreatic cancer models. Nat Commun 2024;15:2192.
54. Dhimolea E, de Matos Simoes R, Kansara D, Al'Khafaji A, Bouyssou J, Weng X, et al. An embryonic diapause-like adaptation with suppressed myc activity enables tumor treatment persistence. Cancer Cell 2021;39:240–56.e11.
55. Duy C, Li M, Teater M, Meydan C, Garrett-Bakelman FE, Lee TC, et al. Chemotherapy induces senescence-like resilient cells capable of initiating AML recurrence. Cancer Discov 2021;11:1542–61.
56. Eddaoudi A, Canning SL, Kato I. Flow cytometric detection of G0 in live cells by Hoechst 33342 and Pyronin Y staining. Methods Mol Biol 2018;1686:49–57.
57. Cibulskis K, Lawrence MS, Carter SL, Sivachenko A, Jaffe D, Sougnez C, et al. Sensitive detection of somatic point mutations in impure and heterogeneous cancer samples. Nat Biotechnol 2013;31:213–9.
58. Saunders CT, Wong WSW, Swamy S, Becq J, Murray L, Cheetham RK. Strelka: accurate somatic small-variant calling from sequenced tumor–normal sample pairs. Bioinformatics 2012;28:1811–7.
59. Hershberg EA, Camplisson CK, Close JL, Attar S, Chern R, Liu Y, et al. PaintSHOP enables the interactive design of transcriptome- and genome-scale oligonucleotide FISH experiment. Nat Methods 2021;18:937–44.
60. Mueller F, Senecal A, Tantale K, Marie-Nelly H, Ly N, Collin O, et al. FISH-quant: automatic counting of transcripts in 3D FISH images. Nat Methods 2013;10:277–8.
61. Tatsumi G, Kawahara M, Yamamoto R, Hishizawa M, Kito K, Suzuki T, et al. LSD1-mediated repression of GFI1 super-enhancer plays an essential role in erythroleukemia. Leukemia 2020;34:746–58.
62. Labun K, Montague TG, Krause M, Torres Cleuren YN, Tjeldnes H, Valen E. CHOPCHOP V3: expanding the CRISPR web toolbox beyond genome editing. Nucleic Acids Res 2019;47:W171–4.
63. Stribbling SM, Ryan AJ. The cell-line-derived subcutaneous tumor model in preclinical cancer research. Nat Protoc 2022;17:2108–28.
64. Loeffler D, Wang W, Hopf A, Hilsenbeck O, Bourgine P, Rudolf F, et al. Mouse and human HSPC immobilization in liquid culture by CD43- or CD44-antibody coating. Blood 2018;131:1425–9.